CHALMERS
UNIVERSITY OF TECHNOLOGY

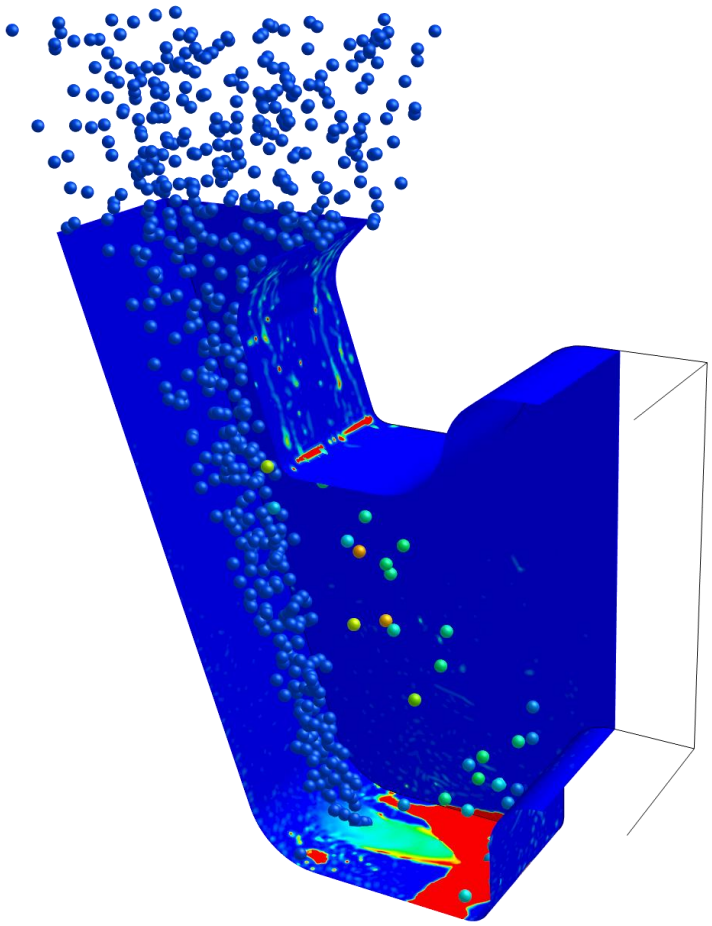

Multiphase CFD simulation of water separation in automotive air intake systems

Master's thesis in Applied Mechanics

ANTON GRANDÉN
JOHAN PERSSON

Department of Mechanics and Maritime Sciences
CHALMERS UNIVERSITY OF TECHNOLOGY
Gothenburg, Sweden 2020

MASTER'S THESIS IN APPLIED MECHANICS

Multiphase CFD simulation of water separation in automotive air intake systems

ANTON GRANDÉN
JOHAN PERSSON

Department of Mechanics and Maritime Sciences
Division of Fluid Dynamics
CHALMERS UNIVERSITY OF TECHNOLOGY

Göteborg, Sweden 2020

Multiphase CFD simulation of water separation in automotive air intake systems
ANTON GRANDÉN
JOHAN PERSSON

Master's thesis 2020:33
Department of Mechanics and Maritime Sciences
Division of Fluid Dynamics
Chalmers University of Technology
SE-412 96 Göteborg
Sweden
Telephone: +46 (0)31-772 1000

Cover:
An illustration of a simplified air intake system with injected water droplets. The color of the droplets represent the size of the droplets and the color of the walls indicates the fluid film thickness.

Chalmers Reproservice
Göteborg, Sweden 2020

Multiphase CFD simulation of water separation in automotive air intake systems
Master's thesis in Applied Mechanics
ANTON GRANDÉN
JOHAN PERSSON
Department of Mechanics and Maritime Sciences
Division of Fluid Dynamics
Chalmers University of Technology

Abstract

Clean and dry air is of the essence for the automotive combustion process as well for the cab climate control systems. Thus, it is important to achieve efficient water separation in the air intake system. Depending on the size and velocity of the water droplets, the water will be separated from the air and exit through the drainage, enter the air intake system or create a thin film on the inner walls of the air intake. This thin film of water might later break up into droplets and once again mix with the air. With a reliable and efficient numerical methodology for prediction of water droplets and water film behavior in the air intake system, it will be possible to optimize the air intakes before any prototypes are built.

To predict the behavior of air and water flow in the air intake systems, two multiphase models in the CFD software STAR-CCM+ were investigated and compared on a simplified geometry. The models used were the Lagrangian Multiphase model (LMP) and the Dispersed Multiphase model (DMP). The investigation was done by conducting several small studies of the LMP and DMP models together with their submodels. Due to its advantages, such as particle tracking and more developed submodels, more time was spent on investigating the LMP model than the DMP model. The Lagrangian Multiphase model was also tested on a complete air intake system. To model the film inside the air intake Fluid Film modelling and Volume of Fluid (VOF) were tested.

Using the results from these studies, together with the findings of the literature review, conclusions were made that the LMP model is more suitable to use for simulate water separation in the automotive air intakes. Due to limitations with the stripping model, VOF could not be used to model the film inside the air intake. Therefore is the Fluid Film model recommended.

The volume fraction of water has a great impact on the percentage of injected water that accumulates in the filter for some droplets diameter. This needs to be taken into consideration when performing simulations and experiments.

Keywords: water separation, automotive air intake, cfd, multiphase, Lagrangian particle tracking, Eulerian-Eulerian, film modelling, impingement, stripping.

Preface

This report describes the masters thesis work performed by Anton Grandén and Johan Persson. The thesis represents the last part of the studies towards a master's degree in Applied Mechanics at Chalmers University of Technology. The work was carried out at Volvo Technology in Gothenburg with supervision from Sassan Etemad and Zenitha Chronéer. The thesis was opposed by Debarshee Ghosh and Mikael Åkerberg and examined by Professor Srdjan Sasic at Chalmers University of Technology.

Acknowledgements

We would like to express our gratitude to the people that have contributed to our work and made this thesis possible. First, we would like to thank our supervisors at Volvo Technology, Sassan Etemad and Zenitha Chronéer, that first of all gave us the opportunity to finish our master's degree with an interesting multiphase flow thesis. But also for supporting us with their knowledge and guidance during the thesis. We also want to thank Johan Forsgren for all the helpful tips on multiphase models and Kurt Nyblom for supporting us during this project and made us feel like a part of the team. In addition, we want to thank all other colleagues at Volvo Technology that have contributed to the thesis with their knowledge and energy.

Furthermore, we would like to express our gratitude to Emil Ljungskog at Siemens for answering our questions and giving helpful guidance about STAR-CCM+. Last but not least, we would like to thank Professor Srdjan Sasic for being our examiner.

Nomenclature

Symbols

α	Volume fraction
$\boldsymbol{\tau}$	Viscous stress tensor
$\boldsymbol{a_{fs}}$	Area surface vector
$\boldsymbol{I}_t$	Identity tensor
$\boldsymbol{S}_{h\boldsymbol{u},imp}$	Source term, momentum due to droplet impingement
$\boldsymbol{S}_{h\boldsymbol{u},sep}$	Source term, Momentum due to film separation
$\boldsymbol{S}_{h\boldsymbol{u}}$	Momentum source term in wall-tangential direction, wall film
$\boldsymbol{S}_h$	Mass source per unit wall area, wall film
$\boldsymbol{T}$	Stress tensor
$\dot{m}$	Mass flow
Γ	Gamma function
λ_{res}	Resonance wave length, wave stripping
μ	Dynamic viscosity
∇	Nabla operator
ν	Kinematic viscosity
ω	Growth rate, edge stripping
ρ	Density
σ	Surface tension
σ_ϵ/σ_k	Model parameter, K-epsilon turbulence model
τ_σ	Contact angle force, film model
τ	Shear stress
τ_c	Eddy transit time
τ_e	Lifetime of eddy
τ_I	Interaction time
τ_v	Particle response time
a	Acceleration
a_0	Splash coefficient, impingement
b	Model parameter for surface tension model, film model
C	Model parameter/Coefficient
C_B	Model parameter for wave stripping, controls rate of break up
C_b	Base coefficient, impingement
C_D	Drag coefficient
c_f	Wall friction coefficient
C_H	Model parameter for wave stripping model, controls how height the film needs to be for stripping to occur
C_R	Model parameter for wave stripping, controls droplet diameter
C_{rd}	Range coefficient for dry wall, impingement

C_{rw}	Range coefficient for wet wall, impingement
d	Diameter
e	Restitution coefficient
E_D	Dissipative energy loss, impingement
$E_{I\sigma}$	Incident droplet surface energy, impingement
E_{KI}	Kinetic energy of the incident normal velocity, impingement
E_{ks}	Splash kinetic energy, impingement
$E_{s\sigma}$	Total energy of splashing droplets, impingement
F	Force
f^D	Form drag force, film model
f_2	Damping function, K-epsilon turbulence model
f_σ	Surface tension force, film model
FR	Force ratio, edge stripping
g	Gravity
h	Film thickness, film model
h_a	Height of film that is stripping
I	Inertia
k	Turbulent kinetic energy
$K^*_{,\infty}$	Gas velocity scaling factor, wave stripping
k_w	Wave number, edge stripping
L	Characteristic length
L_b	Break-up length, edge stripping
La	Laplace number
m_s	Secondary parcel mass
m_π	Impinging parcel mass
N_S	Number of secondary droplets after splash
P	Production term, K-epsilon turbulence model
p	Pressure
p_σ	Pressure from capillary effects, film model
p_g	Gas pressure, film model
p_h	Hydrostatic pressure, film model
p_σ	Capillary pressure, film model
p_{imp}	Droplet impingement pressure, film model
q	Coefficient for Rosin-Rammler distribution
r_m	Ratio between impinging parcel mass and total mass of the secondary parcels
Re	Reynolds number
S	Source terms
St_v	Stokes number
t	Time scale
t_b	Time scale, wave stripping
u	Velocity
u^*	Friction velocity
u_e	Standard deviation

w	Model parameter for surface tension model, film model
We_c	Critical Weber number
We_I	Incident Weber number
X_r	Random number between zero and one, impingement
y	Distance from wall
y^+	Nondimensional wall distance

Subscripts

ϵ	Epsilon-equation
b	Body (external body forces)
c	Continuous phase
D	Drag
d	Dispersed phase
e	Eddy
$film$	Film
imp	Impinging
k	K-equation
$mass$	Mass
n	Normal
r	Relative
s	Surface
t	Tangential
w	Wall

Contents

1 Introduction

This master thesis was carried out at Volvo Technology in Lundby, Gothenburg. Volvo Technology is a part of Volvo Group. Volvo Group is a leading manufacturer of trucks, buses, construction equipment and marine and industrial engines.

1.1 Background

Clean and dry air is of the essence for the combustion process as well for the cab climate control system for heavy duty trucks. Hence, for air purification, usually a cleaner such as a filter is used. It is important to prevent water from entering the air intake system not only because water is undesired in the engine and climate system, but also because it reduces the filter lifespan. The separation can be done before the rain droplets enter the air intake system through the inlet grille. Nevertheless, depending on the size of the droplets, some water might enter the air intake system anyway. Some of this water will create a thin film on the inner walls of the air intake and might later break up into droplets and once again mix with the air. These water droplets might enter the filter.

Today the behavior of air and water flow in air intake systems is investigated through physical testing in a special test rig. For a better understanding of this phenomenon and efficient design of the air intake system, it is desired to develop a reliable numerical methodology for prediction of the water droplets and water film behavior in the air intake system at Volvo Technology. With the numerical method, it will be possible to optimize the air intakes before any prototypes are built.

1.2 Objective

The objective of this project is to establish a simulation methodology to predict the behavior of air and water that is flowing into the air intake system. Transient, multiphase simulations will be needed to capture the behavior. The objective is to validate the simulations with test data from a physical test at Volvo Technology. The purpose of establishing a simulation methodology for the air and water flow is to provide design guidelines for a more efficient water separation system.

The following objectives should be achieved:

- Establishing a simulation methodology for the behavior of air and water in the water separation system of truck air intake systems.
- Provide a comparison between different simulation models.

1.3 Limitations

The limitations of this work are listed below:

- The preferred CFD software nowadays at Volvo Technology is STAR-CCM+ and therefore will only available models in STAR-CCM+ be investigated.
- Only the flow inside and just outside the air intake inlet will be taken into account. Thus, the aerodynamics around the whole truck will not be investigated. The truck will be assumed to have zero velocity.

2 Theory

This chapter provides a theoretical background of multiphase flow and the models used in this project. To begin with, a definition of multiphase flow is stated and an explanation of how different multiphase flows are categorized is given. Later the Eulerian and Lagrangian frameworks, together with some available models are discussed. All models that are described in the theory chapter are implemented in the commercial CFD software STAR-CCM+.

Multiphase flows can be described as a flow with the simultaneous presence of two or more thermodynamic phases, where a phase refers to liquid, solid or vapor state. These flows can be divided into four main categories, gas-liquid, gas-solid, liquid-solid and three-phase flows [17]. The categories together with some examples are given in Table 2.1. Another type of multiphase flow which is not included in the table is the liquid-liquid flow. An example of a liquid-liquid flow is a mixture of oil and water. If the liquids are immiscible the flow cannot be regarded as homogeneous and the liquids are therefore treated as two separate fluids.

Table 2.1: Multiphase flow categories and examples [17].

Gas-liquid flows	Bubbly flows Separated flows Gas-droplet flows
Gas-solid flows	Gas-particle flows Pneumatic transport Fluidized beds
Liquid-solid flows	Slurry flows Hydrotransport Sediment transport
Three-phase flows	Bubbles in a slurry flow Droplets/particles in gaseous flows

Further categorization can be done by the geometrical distribution of the phases. These are called flow regimes or flow patterns and are divided into separated, mixed or dispersed flow. An example of separated flow is a fluid film on a wall with a distinct interface to a gas. Dispersed flow occurs when the dispersed phase is uniformly distributed in the continuous phase. When there exists both separated flow and dispersed flow in the same domain it is called mixed flow.

One example of a multiphase flow that exists in nature is rain. Rain is categorized as a gas-liquid flow with a dispersed flow pattern. Furthermore, rain can be classified into several regimes depending on the intensity. These classifications can be seen in Table 2.2 together with the corresponding average droplet diameter and the liquid water content (LWC). LWC describes the intensity of the rain and is defined as the mass of water contained in a unit volume of air. As the intensity and LWC increases the average droplet diameter increases. Furthermore, water droplets with a diameter less than 2 mm have spherical shape since the surface tension can withstand the pressure from the air as the droplets fall [15].

Single-phase flow is well researched by scientists and engineers and the equations of motion and thermal properties are well acknowledged (Navier-Stokes equations) [17].

However, the study of multiphase flows is considerably less developed due to the complex and collective behavior of a large number of interacting degrees of freedom. This means that the multiphase systems consist of a large number of variables that are dependent on each other. Thus, the governing equations regarding multiphase flow are still under debate.

Table 2.2: Classification and properties of rain according to [6].

Classification	Droplet diameter [mm]	LWC [g/m^3]
Fog	0.01	0.006
Mist	0.10	0.06
Drizzle	0.20	0.09
Light rain	0.45	0.14
Moderate rain	1.0	0.28
Heavy rain	1.5	0.83
Excessive rain	2.1	1.85
Cloudburst	3.0	4-35

2.1 Governing equations in fluid flow

In the continuum mechanics description the motion of fluids can be described with the equation for conservation of mass and the Navier-Stokes equation:

$$\frac{\partial \rho}{\partial t} + \nabla \cdot (\rho \boldsymbol{u}) = 0 \tag{2.1}$$

$$\frac{\partial \rho \boldsymbol{u}}{\partial t} + \nabla \cdot (\rho \boldsymbol{u}\boldsymbol{u}) = -\nabla p + \nabla \cdot \boldsymbol{\tau} + \rho \boldsymbol{g} + \boldsymbol{F}_b \tag{2.2}$$

where ρ is the density of the fluid, $\boldsymbol{u}$ is the instantaneous velocity, p is the pressure, $\boldsymbol{\tau}$ is the viscous stress tensor, $\boldsymbol{g}$ is the gravity and $\boldsymbol{F}_b$ are external body forces. Solving the Navier-Stokes equations without modeling the stress tensor is called direct numerical simulations (DNS). However, turbulent flow is computationally expensive to solve with DNS because a very fine mesh and short time steps are required to solve all turbulence scales. Therefore, turbulence models are introduced in most applications. To predict if the flow is laminar or turbulent the Reynolds number can be used. The Reynolds number is defined as:

$$Re = \frac{\rho u L}{\mu} = \frac{uL}{\nu} \tag{2.3}$$

where L is the characteristic length, μ is the dynamic viscosity and ν is the kinematic viscosity.

2.1.1 Reynolds-Averaged Navier-Stokes (RANS)

Due to the transient behavior of the unsteady turbulent flow, each time dependent property of the flow can be decomposed into a mean value and a fluctuating value as shown below.

$$\phi = \bar{\phi} + \phi' \tag{2.4}$$

where $\bar{\phi}$ is the time averaged value and ϕ' is the fluctuating value. This is known as Reynolds decomposition. Implementing the Reynolds decomposition in equations 2.1 and 2.2 results in the Reynolds-Averaged Navier-Stokes equations shown below:

$$\frac{\partial \rho}{\partial t} + \nabla \cdot (\rho \overline{\mathbf{u}}) = 0 \tag{2.5}$$

$$\frac{\partial}{\partial t}(\rho \overline{\mathbf{u}}) + \nabla \cdot (\rho \overline{\mathbf{u}} \otimes \overline{\mathbf{u}}) = -\nabla \cdot \overline{p}\mathbf{I_t} + \nabla \cdot (\overline{\tau} + \tau_{\mathbf{RANS}}) + \mathbf{F_b}. \tag{2.6}$$

where, ρ is the density, $\mathbf{I_t}$ is the identity tensor, $\overline{\mathbf{u}}$ is the mean velocity vector, $\overline{p}$ is the mean pressure, $\overline{\tau}$ is the mean viscous stress tensor and $\tau_{\mathbf{RANS}}$ is the Reynolds stress tensor.

The correlation between the fluctuating velocities is represented by the Reynolds stress tensor which is an unknown term. The closure problem is that there are more unkowns than equations. Modelling is then used to adress the close problem. One way to close this equation system is by using an eddy-viscosity model which uses the Boussinesq assumption [4].

K-epsilon turbulence model

The k-epsilon model is a so called eddy-viscosity model. With the simplification of the Boussinesq assumption, six turbulent stresses are replaced with one new unknown, the turbulent viscosity. The eddy-viscosity model assumes that the turbulence is isotropic, meaning that the velocity fluctuations will be the same in all directions [4].

The k-epsilon model is a two-equation model. The two equations that are used to solve the transport equation are the modeled k-equations and the modeled epsilon-equation [18]:

$$\frac{\partial}{\partial t}(\rho k) + \nabla \cdot (\rho k \overline{\mathbf{u}}) = \nabla \cdot [(\mu + \frac{\mu_t}{\sigma_k})\nabla k] + P_k - \rho(\epsilon - \epsilon_0) + S_k \tag{2.7}$$

$$\frac{\partial}{\partial t}(\rho \epsilon) + \nabla \cdot (\rho \epsilon \overline{\mathbf{u}}) = \nabla \cdot [(\mu + \frac{\mu_t}{\sigma_\epsilon})\nabla \epsilon] + \frac{1}{T_\epsilon} C_{\epsilon 1} P_\epsilon - C_{\epsilon 2} f_2 \rho (\frac{\epsilon}{T_\epsilon} - \frac{\epsilon_0}{T_0}) + S_\epsilon \tag{2.8}$$

Here is k turbulent kinetic energy, S is a source term, P is a production term, μ is dynamic viscosity, μ_t is the turbulent viscosity, f_2 is a damping function, $\overline{\mathbf{u}}$ is the mean velocity and C respective σ are model parameters.

The k-epsilon model has been widely used in industrial applications and there have been many attempts to improve it. Therefore, there exist countless variants of the k-epsilon model. One of the improved models is the Realizable K-Epsilon model, which is in general better than the standard K-Epsilon for most applications.

2.1.2 Wall treatment

Because of the high velocity gradients in the near wall regions, it is important to resolve or model this region correctly. The walls are also a source of vorticity. There are two different ways to treat wall regions in CFD simulations. The first one is to assume that the logarithmic law is valid and use a coarse mesh in the regions near the walls. This is called a High-Reynolds number model and uses wall functions to model the boundary layer. The second method is to use a fine mesh near the wall to resolve the boundary layer in the viscous region. In the viscous region, the velocity profile is linear. In between, where the linear assumption and the log law are valid, there is a region called the buffer region in where none of the assumptions mentioned above are valid. In Figure 2.1 the linear velocity and the log law are plotted together with experimental data from an open channel flow experiment [13]. The distance from the wall is defined with the nondimensional parameter y^+:

$$y^+ = \frac{y u^*}{\nu} \tag{2.9}$$

where y is the distance from the wall and ν is the kinematic viscosity. u^*, known as friction velocity is defined as:

$$u^* = \left(\frac{\tau_w}{\rho_c}\right)^{1/2} \tag{2.10}$$

where τ_w is the wall shear stress.

One problem is that turbulence models like K-Epsilon are not valid in the viscous dominating region near the walls. Therefore, when using the second approach the turbulence model needs to be modified. The modified models are called Low-Reynolds number models [4].

There are alternative approaches to the Low-Reynolds number model like the Two-Layer approach. With the Two-Layer approach, the k-epsilon model can be used near the walls as well. This can be done because the computation is divided into two layers. The turbulent viscosity and the turbulent dissipation are functions of the distance to the wall in the near wall regions. The turbulent kinetic energy is solved across both layers. The Two-Layer approach is often more accurate than the Low-Reynolds number model[18].

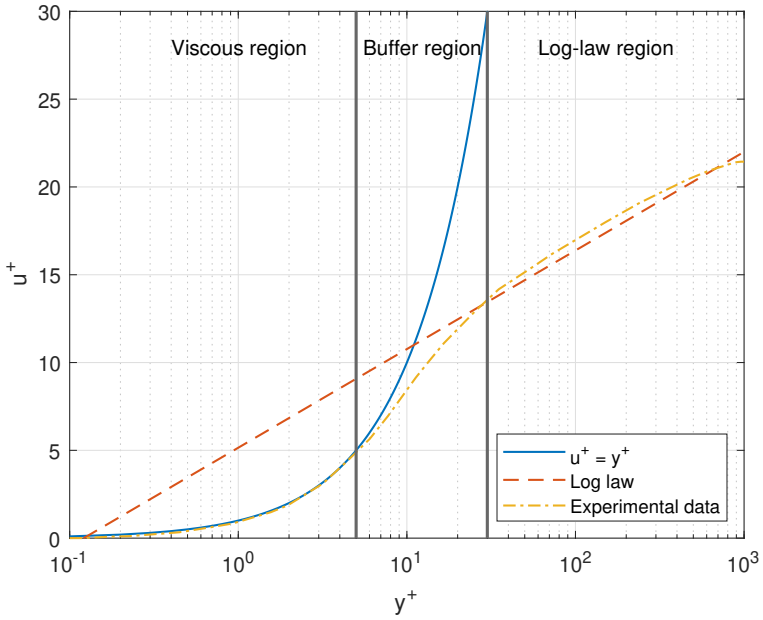

Figure 2.1: Wall boundary layer with the three regions near the wall plotted together with wall models compared to experimental data [13].

2.2 Frame of reference

Two frequently used frameworks in fluid dynamics are Eulerian and Lagrangian. The Eulerian frame of reference use control volumes which are fixed in space to study the motion of the fluid as it passes with time. The Lagrangian frame of reference moves with the flow. The observer follows one individual fluid particle as it moves through space and time. The models described later are based on either the Eulerian framework, the Lagrangian framework or a combination of them. These modeling approaches have been developed for different types of flow patterns as well as with different levels of accuracy and computational costs.

The Eulerian-Lagrangian approach is a method that uses both the Eulerian and the Lagrangian framework. The Eulerian framework is used to represent the carrier phase and the Lagrangian framework is used to track the dispersed phase. With this approach, it is possible to track each individual particle in a carrier fluid.

The Eulerian-Eulerian (also called multi-field and multi-fluid modeling) approach uses the Eulerian framework for both the carrier phase and the dispersed phase. Using this approach one has to assume that the particles (the dispersed phase) are a continuous interpenetrating continua. This assumption introduces stresses, more specifically, contact and streaming stresses. When representing the particles as a continuous cloud, one does not solve for the motion of each individual particle. Therefore, this approach has considerably lower computational costs compared to the Eulerian-Lagrangian approach.

2.3 Lagrangian Multiphase (LMP)

Lagrangian Multiphase model is a model that uses the Euler-Lagrangian approach [18]. The particles can either be real or modeled as massless point sources. Instead of tracking each particle, several particles are represented in groups called parcels, this makes the model less computationally expensive. The parcels are tracked by solving the Lagrangian equations of conservation of mass, momentum and energy, whereas the continuous phase is solved with the Navier-Stokes equations. The coupling between the phases can be one-, two- or four-way coupled. An overview of the couplings is illustrated in Table 2.3. The volume fraction of the dispersed phase of the flow can be used to decide the phase coupling. The volume fraction of phase i is defined according to equation 2.11.

$$\alpha_i = \frac{V_i}{V} \tag{2.11}$$

where V is the total volume and V_i is the volume of phase i. For dense flows, that is when the volume fraction is of the order of 10^{-3} or above, particle-particle collisions and contacts can't be neglected and four-way coupling

is desired [8]. Flows with volume fraction lower than 10^{-3} are said to be dilute and one- or two-way coupling is sufficient. A volume fraction of 10^{-6} is occasionally used for the limit between one- and two-way coupling. For volume fraction lower than 10^{-6} one-way coupling is sufficient but for higher volume fraction than 10^{-6}, two-way coupling is needed.

Table 2.3: Coupling approaches between the continuous and dispersed phase.

One-way	Particles do not affect the continuous phase Particles do not affect each other Particles moved by the continuous phase
Two-way	Particles affect the continuous phase Particles do not affect each other Particles moved by the continuous phase
Four-way	Particles affect the continuous phase Particle-Particle interaction taken into account Particles moved by the continuous phase

In the one-way coupling approach, the carrier phase influences the droplets with a momentum coupling but the droplets do not affect the carrying fluid. The coupling is modeled by identification of the forces acting on the particles. The properties of the phases determine which forces are important for a certain case. For water droplets dispersed in air, the dominant force is the drag force, which can be expressed as:

$$\boldsymbol{F_D} = \frac{1}{2}\rho_c \frac{d_d^2 \pi}{4} C_D |\boldsymbol{u_c} - \boldsymbol{u_d}|(\boldsymbol{u_c} - \boldsymbol{u_d}) \tag{2.12}$$

where C_D is the drag coefficient. There exist multiple correlations for the drag coefficient. One correlation which is suitable for liquid droplets is the Schiller-Naumann correlation [18] which can be seen in equation 2.13 where Re_d is the particle Reynolds number and is defined according to equation 2.14.

$$C_D = \begin{cases} \frac{24}{Re_d}\left(1 + 0.15 Re_d^{0.687}\right) & \text{if } Re_d \leq 10^3 \\ 0.44 & \text{if } Re_d > 10^3 \end{cases} \tag{2.13}$$

$$Re_d = \frac{\rho_c |\boldsymbol{u_c} - \boldsymbol{u_d}| d_d}{\mu_c} \tag{2.14}$$

The continuity and momentum equations in the Eulerian framework for the carrier phase can be written as:

$$\frac{\partial}{\partial t}(\alpha_c \rho_c) + \nabla \cdot (\alpha_c \rho_c \boldsymbol{u_c}) = S_{mass} \tag{2.15}$$

$$\frac{\partial}{\partial t}(\alpha_c \rho_c \boldsymbol{u_c}) + \nabla \cdot (\alpha_c \rho_c \boldsymbol{u_c} \boldsymbol{u_c}) = -\alpha_c \nabla \rho_c - \nabla \cdot (\alpha_c \boldsymbol{\tau_c}) - S_d + \alpha_c \rho_f \boldsymbol{g} \tag{2.16}$$

where α_c, ρ_c and $\boldsymbol{u_c}$ are the volume fraction, the density and the velocity of the carrier phase respectively. S_{mass} and S_d are mass and momentum transfer between the carrier fluid and each particle. Equation 2.17 and 2.18 describe the momentum equation and the rotation equation in the Lagrangian framework for the dispersed phase.

$$m_d \frac{d\boldsymbol{u}_d}{dt} = \sum \boldsymbol{F} \tag{2.17}$$

$$I_d \frac{d\omega_d}{dt} = \boldsymbol{T_d} \tag{2.18}$$

where m_d and $\boldsymbol{u_d}$ are the particle mass and velocity. $\sum \boldsymbol{F}$ is the sum of all particle forces. I_d is the particle inertia and ω_d is the particle angular velocity. $\boldsymbol{T_d}$ is the rotating force acting on the particle such as rotating drag, particle rolling resistance.

In a two-way coupled simulation the droplets influence the carrier fluid. This is done by adding source terms in the equations for the continuous phase. This means that the particles are not solved in the Eulerian field. The interaction between them is modeled.

The Lagrangian equations can be solved for every single particle. However, if the number of particles is large, this will require a lot of computational resources. Instead, particles are represented in clouds consisting of multiple particles. These are called parcels or computational particles. All the particles in a parcel are assumed to have the same properties (velocity, size, rotation rate) [18].

2.3.1 Turbulent dispersion

Particle dispersion occurs due to fluctuating fluid forces that are continuous and vary in magnitude throughout the flow field [17]. Since no turbulent dispersion is created by mean fields and the RANS results in mean fields, this needs to be modeled. For small particles, the particles follow the instantaneous motion of the carrier phase, hence the particle dispersion is equal to the fluid dispersion. However, due to their greater inertia, larger particles do not follow the fluctuating motion of the fluid to the same extent.

Many models have been suggested to simulate particle dispersion. One of them was introduced by Gosman and Ioannides [7], which uses a stochastic approach were every particle travels through a sequence of turbulent eddies as it flows through a turbulent flow field. In every eddy, the particle is affected by the instantaneous velocity of the fluid. This instantaneous velocity can be written as:

$$\boldsymbol{u} = \overline{\boldsymbol{u}} + \boldsymbol{u}' \tag{2.19}$$

where $\overline{\boldsymbol{u}}$ is the mean field velocity from RANS and $\boldsymbol{u}'$ is the fluctuating velocity component. This velocity is modeled using a Gaussian distribution with zero mean and a standard deviation given by the eddy velocity scale u_e.

$$u_e = \frac{L}{t}\sqrt{\frac{2}{3}} \tag{2.20}$$

L and t are the length and time scale of the turbulence, respectively. For k-epsilon and k-omega turbulence models, the ratio L/t is equal to the square root of the turbulent kinetic energy ($\sqrt{k}$). The time the particle is inside an eddy is called the interaction time and is defined according to equation 2.21, where τ_c is the eddy transit time and is equal to the time the particle is inside an eddy due to the relative velocity between the particle and the eddy, see formula 2.22. τ_e is the lifetime of the eddy, see equation 2.23.

$$\tau_I = min(\tau_e, \tau_c). \tag{2.21}$$

$$\tau_c = \begin{cases} \infty & \text{if } \tau_v \leq \frac{l_e}{|\boldsymbol{v}_s|} \\ -\tau_v \ln\left(1 - \frac{l_e}{\tau_v |\boldsymbol{v}_s|}\right) & \text{if } \tau_v > \frac{l_e}{|\boldsymbol{v}_s|} \end{cases} \tag{2.22}$$

$$\tau_e = \frac{2\mu_t}{\rho u_e^2} \tag{2.23}$$

Here, τ_v is the momentum relaxation time scale and l_e is the eddy length scale.

2.4 Volume Of Fluid (VOF)

The Volume of Fluid (VOF) multiphase model uses the Eulerian-Eulerian framework which means that both phases are treated as continuous. VOF uses an implicit interface capturing method to predict the interface between the immiscible phases [18]. This is done by a phase indicator function, e.g. the volume fraction (see equation 2.11). The phase indicator function α_i, is equal to unity if the cell is fully filled with the phase i and equal to zero if the cell is fully void of phase i. If there is an interface present in the cell the phase indicator function is between zero and one. Furthermore, the sum of the volume fractions of the phases is equal to unity. The interface is tracked by solving the equation 2.24 [16].

$$\frac{\partial \alpha}{\partial t} + \nabla \cdot (\alpha \boldsymbol{u}) = 0 \tag{2.24}$$

When there are two phases present, equation 2.24 is only solved for the first phase. Then the volume fraction of the second phase is adjusted so that the sum of the two is equal to one [18]. Furthermore, the continuity and momentum equation used in VOF are shown below [16].

$$\frac{\partial \rho}{\partial t} + \nabla \cdot (\rho \boldsymbol{u}) = 0 \tag{2.25}$$

$$\frac{\partial \rho \boldsymbol{u}}{\partial t} + \nabla \cdot (\rho \boldsymbol{u}\boldsymbol{u}) = \nabla \cdot \boldsymbol{T} + \rho \boldsymbol{g} + \boldsymbol{F}_b \tag{2.26}$$

Here is $\boldsymbol{T}$ is the stress tensor. To be able to resolve the position and shape of the interface between the phases, the mesh resolution needs to be very high. Thus, this modeling approach is computationally expensive.

2.5 Dispersed Multiphase (DMP)

The Dispersed Multiphase model uses the Eulerian framework for both the continuous and dispersed phases and is suitable for flows with low volume fraction [18]. For cases when the trajectory of individual particles are not of interest, DMP is an alternative to the Lagrangian Multiphase model due to its low computational costs. By default, DMP is one-way coupled but is compatible with two-way coupling simulations where drag forces and heat transfer are taken into account in both the dispersed phases and the continuous phase. The main difference between DMP and a traditional multi-field approach such as the Eulerian Multiphase (EMP) model in STAR-CCM+ is that in DMP the continuous background phase is solved with a typical single-phase model.

For the dispersed phases, the equations of mass and momentum conservation are solved as shown below.

$$\frac{\partial (\alpha_i \widetilde{\rho}_i)}{\partial t} + \nabla \cdot (\alpha_i \widetilde{\rho}_i \overline{\boldsymbol{u}}_i) = S_{u,i} \tag{2.27}$$

$$\frac{\partial}{\partial t}(\alpha_i \widetilde{\rho}_i \overline{\boldsymbol{u}}_i) + \nabla \cdot (\alpha_i \widetilde{\rho}_i \overline{\boldsymbol{u}}_i \overline{\boldsymbol{u}}_i) = -\nabla(\alpha_i \widetilde{p}_i) + \boldsymbol{F_D} + S_{u,i} \tag{2.28}$$

$S_{u,i}$ is the mass source respective momentum source for the dispersed phase i and $\boldsymbol{F}_D$ is the drag force acting on the dispersed phase i from phase j and is defined as:

$$\boldsymbol{F_D} = \frac{1}{2} C_D \frac{6\alpha_d}{4d} \rho_d |\boldsymbol{u_c} - \boldsymbol{u_d}| (\boldsymbol{u_c} - \boldsymbol{u_d}) \tag{2.29}$$

C_D represents the drag force and was explained in section 2.3. α_d is the volume fraction of the particles, ρ and d are the density and the diameter of the particle respectively. $\boldsymbol{v_r}$ is the relative velocity between the particles and the continuous phase.

The advantage with DMP is the low computational costs compared to LMP since one does not solve the motion of each individual particle. The drawback is that it does not support as complex physics as LMP or EMP. For example, turbulent dispersion, particle-particle interaction, evaporation and complex wall interaction are not supported.

Convergence can be an issue for DMP and other Eulerian-Eulerian multiphase models. This is caused by the strong coupling between the phases and therefore the conservation of momentum. Also, the conservation of mass is difficult to secure. To secure the conservation of mass the solution may need to transfer mass between the phases which can be unphysical. To minimize the divergence issues it is often recommended to use low under-relaxations factors and small time steps, which increases the computational cost.

2.6 Particle-wall interaction

For pipe flows or similar, particle wall interaction is important if the dispersed phase does not follow the direction changes of the continuous phase. The Stokes number, equation 2.30, is a useful parameter to approximate if the dispersed phase will follow the continuous phase. τ_v is the particle response time and t is the characteristic time scale of the flow. If $St_v << 1$ the dispersed phase will follow the continuous phase. If $St_v >> 1$ the dispersed phase will not have time to change the direction and may clash with a wall [17].

$$St_v = \frac{\tau_v}{t} \tag{2.30}$$

The particle response time is defined in equation 2.31. ρ_d and d_d are the density and diameter of the dispersed phase respectively. μ_c is the dynamic viscosity of the continuous phase.

$$\tau_v = \frac{\rho_d d_d^2}{18 \mu_c} \tag{2.31}$$

2.6.1 Wall impingement

An impact of a droplet on a solid wall can result in several different effects, e.g. *splash*, *spread*, *rebound* and *adhere*. These effects depend on the size, velocity and material of the droplet, but also on the temperature of the wall and if it is wet or dry [18]. One of the models for simulation of this behavior is the Bai-Gosman model [2], which has later been improved and extended in [1] and [3]. The Bai-Gosman model is possible to use with the LMP model but is not feasible with the DMP model. The six outcomes of a droplet-wall impingement can be seen in Figure 2.2. According to this model, the outcome depends on the incident Weber number (equation 2.32), the Laplace number (equation 2.33), the temperature of the wall and if the wall is wet or dry.

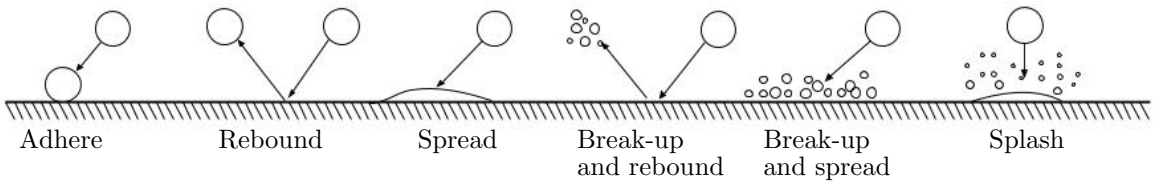

Figure 2.2: Bai-Gosman wall impingement effects.

$$We_I = \frac{\rho_d u_{r,n}^2 d_d}{\sigma} \tag{2.32}$$

$$La = \frac{\rho_d \sigma d_d}{\mu_d^2} \tag{2.33}$$

where $u_{r,n}^2$ is the droplet normal incident velocity and σ is the surface tension.

Figure 2.3 illustrates the regimes for the different outcomes depending on the incident Weber number for dry and wet walls when the wall temperature is below the boiling temperature of the droplet. The regimes *break-up* and *rebound/spread* will only occur for wall temperatures above the boiling temperature. Therefore, those regimes will not be further discussed.

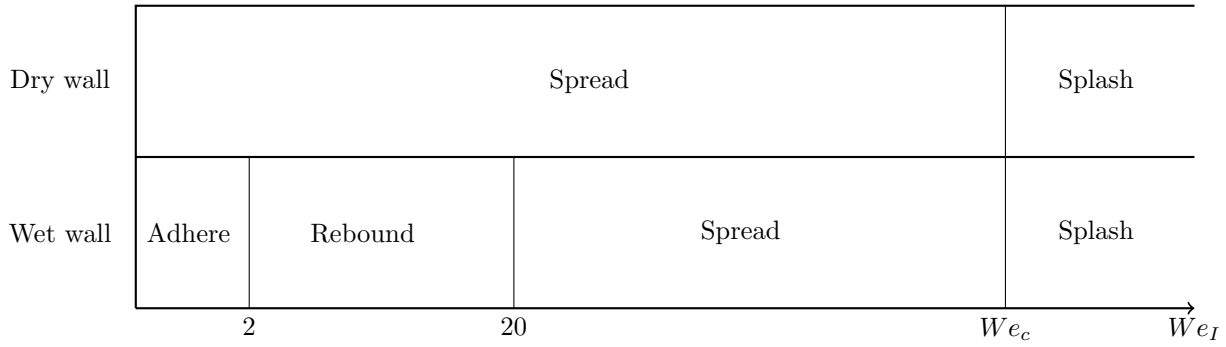

Figure 2.3: Bai-Gosman wall impingement regimes for wet and dry walls when the wall temperate is below the droplets boiling temperature.

Adhere is when a droplet sticks to the wall in an almost spherical shape. This regime exists only for wet walls and when the incident Weber number is below two [3]. Furthermore, at impingement on wet walls, the lost mass, momentum and kinetic energy of the droplets will be transferred to the fluid film.

Rebounds will only occur for wet walls when $2 < We_I < 20$. This outcome, as Figure 2.2 illustrates, is when the droplet bounces back into the domain and loses some of its kinetic energy. The tangential and normal velocities after the *rebound* are calculated according to equation 2.34 and 2.35 where the superscript ' represents the velocity after impact. The tangential restitution coefficient, e_t, is equal to 5/7 and the normal restitution coefficient e_n are calculated according to equation 2.36, where θ is the droplet incident angle.

$$\mathbf{u_t'} = \mathbf{e_t u_t} \tag{2.34}$$

$$\mathbf{u}_\mathbf{n}' = -\mathbf{e}_\mathbf{n}\mathbf{u}_\mathbf{n} \tag{2.35}$$

$$e = 0.993 - 1.76\theta + 1.56\theta^2 - 0.49\theta^3 \tag{2.36}$$

For dry walls, *spread* will occur when $We_I < We_c$ and for wet walls when $20 < We_I < We_c$, where $We_c = ALa^{-0.18}$ and A is a coefficient that depends on the surface roughness. The *spread* outcome results in a fluid film that is formed by the droplet. Data for A, from an experiment with a dry wall by Stow and Hadfield is tabulated in Table 2.4 [19]. According to the experiment, the coefficient decreases with increasing surface roughness. In other words, increased surface roughness will increase the probability of *splashing* to occur on a dry wall. For a wetted wall, a coefficient of 1320 is suggested, corresponding to a very rough wall. The outcome in this regime can be modeled as the *rebound* regime with equation 2.34 and 2.35 but with restitution coefficients $e_t = 1$ and $e_n = 0$.

Table 2.4: A as a function of the surface roughness, r_s, for dry wall [19].

r_s	A
0.05	5264
0.14	4534
0.84	2634
3.1	2056
12	1322

For both dry and wet walls, the droplet will *splash* when $We_c < We_I$. For *splash*, the droplet breaks up into a random number of smaller droplets with random diameters, while a fraction of the original droplet might remain stuck on the wall to form a fluid film. The number of secondary droplets and their diameters are selected using a Rosin-Rammler distribution. These droplets are reflected back into the domain as a cone injector with velocities calculated using the conservation of energy.

Once an impinging parcel *splash* against a wall, a specified number of secondary parcels are produced. According to [3], a good compromise between cost and accuracy is to use two secondary parcels. From equation 2.37 the ratio between the impinging parcel mass m_π and the total mass of the secondary parcels m_s can be calculated.

$$r_m = \frac{m_s}{m_\pi} = C_b + \binom{C_{rd}}{C_{rw}} X_r \tag{2.37}$$

where C_b is the base coefficient, C_{rw} is the range coefficient for wet walls, C_{rd} is the range coefficient for dry walls and X_r is a random number between 0.0 to 1.0. According to Bai [1], C_b, C_{rd} and C_{rw} can be approximated to be 0.2, 0.6 and 0.9 respectively, to agree with experimental data. For wetted walls, $C_b + C_{rw}$ can be larger than 1. This is because *splashing* may entrain liquid from the fluid film, which has been observed in some experiments. The mass of water that sticks to the wall is equal to $(1 - r_m)m_\pi$.

To calculate the number of droplets that are created after a *splash* equation 2.38 is used.

$$N_S = a_0\left(\frac{We_I}{We_c} - 1\right) \tag{2.38}$$

where the coefficient a_0 is suggested to be 5.0 to match experimental data according to Bai [1].

A Rosin-Rammler distribution is used to ensure random diameters of the secondary droplets togheter with a reference diameter:

$$d_{ref} = \left(\frac{r_m}{N_s\Gamma(1 + 3/q)}\right)^{1/3} d_d \tag{2.39}$$

where q is a coefficient that modifies the distribution, q=1.0 result in a Chi-squared distribution. The symbol Γ represents the gamma function which is an extension of the factorial function.

The absolute velocity of the secondary droplets can be divided into two components as shown in equation 2.40, where the superscript ' represents the state after the impingement. The velocities $\mathbf{u}_\mathbf{t}'$ and $\mathbf{u}_\mathbf{n}'$ are due to the tangential and normal incident velocity, $\mathbf{u}_\mathbf{t}$ and $\mathbf{u}_\mathbf{n}$, respectively.

$$\mathbf{u}' = \mathbf{u}_\mathbf{t}' + \mathbf{u}_\mathbf{n}' \tag{2.40}$$

The tangential velocity of the secondary droplets, $\mathbf{u'_t}$, is calculated as:

$$\mathbf{u'_t} = \mathbf{c_f u_t} \tag{2.41}$$

where c_f is the wall friction coefficient. This coefficient is estimated to be in the range of 0.6 to 0.8 [3].

Determining the velocity of the secondary droplet i, $\mathbf{V'_{n,i}}$, due to the normal incident velocity is far from trivial. The velocity can be defined by three parameters; the azimuthal angle ϕ, the ejection angle θ and the magnitude of the velocity. The angles are defined as shown in Figure 2.4 where the wall is located in the x-y plane. Note that the velocity due to the normal incident velocity is not in general normal to the wall. The azimuthal angle ϕ is randomly selected in the range of 0° to 360° with equal probability [3]. The ejection angle θ can be in the range of a minimal bounding angle θ_b° and a maximal bounding angle 90°. The minimal bounding angle depends on the thickness of the film or the surface roughness. There is not an equal probability for the ejection angle in the range of θ_b° to 90°. Many different sub-ranges with higher probabilities have been suggested. The range used in [3] is 5° to 50°, furthermore, the probability of an ejection angle outside this range is so low it is removed from the possible outcome.

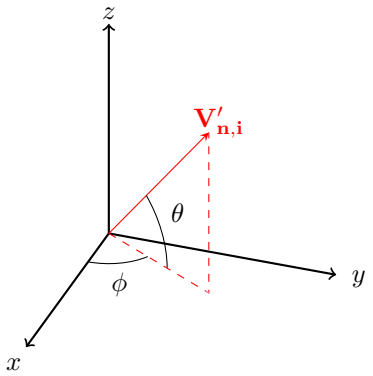

Figure 2.4: Velocity of the secondary droplet i due to the normal incident velocity. The wall is located in the x-y plane.

The magnitude of the normal velocity, $u'_{n,i}$, is calculated from the conservation of energy, including all the secondary parcels, according to:

$$\frac{1}{2}\frac{m_s}{p}\Big[(u'_{n,1})^2 + ... + (u'_{n,p})^2\Big] = E_{KS} \tag{2.42}$$

where p is the number of secondary parcels. E_{KS} is called splash kinetic energy which is calculated as shown in equation 2.43 where E_{KI} is the kinetic energy of the incident normal velocity, $E_{I\sigma}$ and $E_{S\sigma}$ are the incident droplet surface energy and total surface energy of splashing droplets respectively. E_D is the dissipative energy loss defined according to equation 2.44.

$$E_{KS} = E_{KI} + E_{I\sigma} - E_{S\sigma} - E_D. \tag{2.43}$$

$$E_D = \max\Big(0.8E_{KI}, \frac{We_c}{12}\pi\sigma d_I^2\Big) \tag{2.44}$$

If there is more than one secondary parcel, in other words, if $p > 1.0$, an additional equation is needed to solve the velocities of all the parcels:

$$\Big(\frac{u'_{n,1}}{u'_{n,i}}\Big) \approx \ln\Big(\frac{d_1}{d_I}\Big)/\ln\Big(\frac{d_i}{d_I}\Big) \quad (i = 2, ..., p) \tag{2.45}$$

As explained before, the Bai-Gosman wall impingement model is not feasible with the DMP model. Instead, there exists a simplified wall impingement model for the DMP model. In the simplified model, all the droplets that get in contact with the wall are transferred to fluid film. This includes the mass, momentum and energy of the impinging droplet.

The droplets transferred from the dispersed phase to the film can be calculated as:

$$\dot{m}_{imp} = \rho \boldsymbol{u} \cdot \boldsymbol{a}_{fs} \tag{2.46}$$

Here $\dot{m}_{imp}$ is the mass flux that impinginges, ρ is the density, $\boldsymbol{u}$ is the velocity vector and $\boldsymbol{a}_{fs}$ is the area vector of the surface.

2.6.2 Wall film

When droplets clash with a wall they will wet it and a thin fluid film will be built up. This is due to the adhesion forces between the water molecules and the wall and the cohesive forces between the water molecules [9].

The film interface can be solved with for example the Volume of Fluid method or modeled with film modeling. The film model solves the equations for continuity, transport, energy, species and volume fraction in the Eulerian framework. The fluid film is assumed to be laminar and has a parabolic velocity profile with a no-slip boundary condition at the wall. The film is modeled with a region that is only one cell thick [18]. This can be done due to the so called thin-film assumption which states that diffusion is considered in the wall-normal direction and advection in the wall-tangential direction. But at sharp corners, the approximation breaks down [14]. However, the assumption allows integration over the whole film height in the wall-normal direction to obtain the continuity and momentum equation [12].

The continuity equation that is solved is:

$$\frac{\partial \rho_{film} h}{\partial t} + \nabla_s [\rho_{film} h \boldsymbol{u}] = S_h \tag{2.47}$$

where ρ_{film} is the density of the liquid film, h is the film thickness and $\boldsymbol{u}$ is the film velocity. ∇_s represents the vector differential operator tangential to the surface. The mass source per unit wall area term S_h is dependent on the relevant physics. It can for example consist of droplet impingement, film separation, mass transfer, etc.

The momentum equation is:

$$\frac{\partial \rho_{film} h \boldsymbol{u}}{\partial t} + \nabla_s [\rho_{film} h \boldsymbol{u}\boldsymbol{u}] = -h \nabla_s p + \boldsymbol{S}_{h\boldsymbol{u}} \tag{2.48}$$

The terms $-h\nabla_s p$ and $\boldsymbol{S}_{h\boldsymbol{u}}$ are the source terms for the momentum equation, this terms are also dependent of the relevant physics. The first source term, $-h\nabla_s p$, is treated in the wall-normal direction and can include hydrostatic pressure (p_h), pressure from the gas (p_g), capillary effects (p_σ) and droplet impingement pressure (p_{imp}), see equation 2.49. The second source term, $\boldsymbol{S}_{h\boldsymbol{u}}$, is treated in the wall-tangential direction and can include gravity force ($\rho \boldsymbol{g}_t h$), contact angle force (τ_σ), viscous shear stresses from gas and wall (τ_g and τ_w) and momentum due to droplet impingement ($\boldsymbol{S}_{h\boldsymbol{u},imp}$) and film separation($\boldsymbol{S}_{h\boldsymbol{u},sep}$), see equation 2.50.

$$p = p_h + p_g + p_\sigma + p_{imp} \tag{2.49}$$

$$\boldsymbol{S}_{h\boldsymbol{u}} = \rho \boldsymbol{g}_t h + \tau_\sigma + \tau_g + \tau_w + \boldsymbol{S}_{h\boldsymbol{u},imp} + \boldsymbol{S}_{h\boldsymbol{u},sep} \tag{2.50}$$

Pressure variations over the film can be caused by gas flowing over the film surface. The form drag force is a model that tries to model the integrated net force on the film caused by those pressure variations. The net force is added to the momentum equation of the fluid film, equation 2.48, and is calculated as [18]:

$$\boldsymbol{f}^D = C_D \frac{\rho}{2} \boldsymbol{u}^2 A \tag{2.51}$$

In the equation above, C_D is the drag coefficient, ρ is the gas density, $\boldsymbol{u}^2$ is the velocity of the gas and A is the area.

At the interface between the gas phase and the fluid film, there is surface tension. The surface tension arises from the cohesive forces between the water molecules that are greater than the adhesion forces between the water molecules and the air molecules [18]. According to [12], the surface tension can be divided into its normal and tangential components as:

$$\boldsymbol{f}_\sigma = p_\sigma \boldsymbol{n} + \boldsymbol{\tau}_\sigma \tag{2.52}$$

where p_σ is the capillary pressure and $\boldsymbol{\tau}_\sigma$ is the contact angle force.

The capillary pressure is the wall-normal component of the surface tension. For surfaces with slight curvature the capillary pressure can be written as:

$$p_\sigma = -a\sigma\nabla_s^2 h \tag{2.53}$$

where σ is the surface tension coefficient, $\nabla_s^2 h$ approximates the curvature of the film surface and the term a is a non-dimensional scale factor used to tune in the model.

The contact angle force is the wall-tangential component of the surface tension and limits the film from spreading. The force is applied along the contact line, which is the delineation between the dry and wet regions. Film behavior such as dry spots and rivulets are described by this force which can be written as:

$$\tau_\sigma = b\sigma(1 - \cos(\theta))\nabla w \tag{2.54}$$

where θ is the contact angle and b is an empirical non-dimensional parameter used to tune in the model with respect to experimental results. By experimental measure the critical film flow, the parameter b can be adjusted so that the model has the same critical film flow, where the critical film flow is defined as the point where film rivulets merge to a continuous film. The parameter w in the equation is equal to 1.0 for wet regions and 0.0 for dry regions. The value of w depends on the critical film thickness, which is the threshold between the dry and wet region and can be defined as the value at below which no stable film exists.

Wave stripping

The film can sometimes break up into droplets. This can happen due to body forces, forces from the adjacent fluid flow or the wall geometry. If the droplets are formed due to body forces or forces from the adjacent fluid flow it is called wave stripping.

The wave stripping is based on the Rayleigh-Taylor instability theory. The volume of the ejected fluid is formed as a cylinder according to Kelvin-Helmholtz instability. Due to the Rayleigh-Taylor instabilities, the cylinder then breaks into droplets. From the most unstable wavelength that characterizes the surface instability, the child droplet radius is calculated. The resonance wave length is calculated as:

$$\lambda_{res} = \frac{2\pi}{\rho_{film}\boldsymbol{f_b}\cdot\boldsymbol{n}}\left(\frac{1}{3}\rho_c\widetilde{\boldsymbol{u}}_r^2 - \sqrt{\left(\frac{1}{3}\rho\widetilde{\boldsymbol{u}}_r^2\right)^2 - \rho_{film}\boldsymbol{F_b}\cdot\boldsymbol{n}\sigma}\right) \tag{2.55}$$

where $\boldsymbol{F}_b$ is the body force, σ is the surface tension and $\widetilde{\boldsymbol{u}}$ is the relative velocity between the surrounding fluid and the film. For droplet ejection, the necessary film height is calculated as:

$$h_{min} = C_H\frac{\lambda_{res}}{2\pi} \tag{2.56}$$

where the parameter C_H controls how thick the fluid film needs to be for stripping to occur. The height of the film that goes to be stripped is calculated as:

$$h_a = \left[\frac{3}{4}\left(\frac{2}{3.78}\right)^3\right]^2\pi\lambda_{res} \tag{2.57}$$

and the diameter of the droplet that is created from the stripping is calculated as:

$$d_d = C_R\sqrt{\frac{\lambda_{res}h_a}{\pi}} \tag{2.58}$$

Where the parameter C_R is normally 3.78 from the Rayleigh theory. According to the formula, the droplet diameter is C_R times the diameter of the ejected cylinder. However, when using the DMP model the wave stripping works a bit different. Only one particle diameter is allowed for each phase. Consequently, the diameter of the stripped droplets is not calculated when the stripping occurs, but selected before. Furthermore, when the droplets are ejected they initially have the same velocity as the film.

The number of times stripping occurs during a time step is then calculated as:

$$n_b = C_B\frac{\Delta t}{t_b} \tag{2.59}$$

where C_B is used to control the rate of breakup and the time scale t_b can be defined as:

$$t_b = \frac{\lambda_{res}(\rho_{film} + \rho_c)}{|u_r|\sqrt{(1 - We)\rho_{film}\rho_c}} \tag{2.60}$$

where the Weber number, We, is equal to 2/3. This is the Weber number when the most unstable mode occurs.

For the wave stripping model, the free stream-velocity of the surrounding gas is needed. The velocity can be calculated in two different ways. It can be calculated in the nearest gas cell. This method is mesh dependent and the validity decreases with a decreasing mesh size. The second method is to estimate the velocity based on the shear velocity. This is mesh independent.

For the second method, the shear velocity is calculated as:

$$\boldsymbol{u^*} = -\sqrt{\frac{\tau}{\rho_c}}\boldsymbol{n}_\tau \tag{2.61}$$

Where n_τ is the unit vector in the direction of the shear stress τ. The free stream gas velocity can then be approximated as:

$$\boldsymbol{u_r} \approx (\boldsymbol{u})_{int} + K^*_{,\infty}\boldsymbol{u}^* = \boldsymbol{u} \tag{2.62}$$

The parameter $K^*_{,\infty}$ is the gas velocity scaling factor and $(\boldsymbol{u})_{int}$ is the velocity at the interface [18].

Edge stripping

If the film is driven over a sharp edge, break up can occur. Droplets are formed when the film is forced over the edge. Modeling of the break up over a sharp edge is called edge stripping.

The edge stripping can be simulated based on a force balance model by Friedrich et al [5] and the droplet size distribution model by [10]. When the liquid film flows over a corner it may remain attached to the wall or be separated from the wall and break up into droplets by the aerodynamic forces. The forces included in the model are inertia, gravitational effects and surface tension. As the film flows over a corner the momentum of the film drives the separation from the wall. This effect is balanced by the surface tension and the gravitational force. The force ratio (FR) is used to determine if separation will occur at a corner and is calculated as:

$$FR = \frac{We_{film}}{1 + \frac{1}{sin\theta} + Fr_{h,film}We_{film}\left(\frac{L_b}{h_{film}}\right)\left(\frac{1}{tan\theta}\right)} \tag{2.63}$$

where $We_{film} = \rho_{film}u^2_{film}h_{film}/\sigma$, $Fr_{h,film} = gh_{film}/u^2_{film}$ and $Re_{film} = \rho_{film}u_{film}h_{film}/\mu_{film}$. Furthermore, u_{film} is the velocity of the film projected orthogonal to the stripping edge, h_{film} is the height of the film and θ is the corner angle at the edge. L_b in equation 2.63 is called break-up length and is defined as:

$$L_b = 0.0388h^{0.5}_{film}Re^{0.6}_{film}We^{-0.5}_{rel} \tag{2.64}$$

where $We_{rel} = \rho_{film}(u_g - u_{film})^2h_{film}/2\sigma$ and u_g is the velocity of the surrounding gas.

Once the force ratio (FR) becomes greater than the critical force ratio ($\mathrm{FR_C}$) the inertial force is large enough for the film to start to separate from the wall. The force ratio is also used to determine how large fraction of the film that is being separated. To approximate this fraction, x_s, the following formula is used which is based on experimental data [5]:

$$x_s = \begin{cases} 0 & \text{if } \mathrm{FR} \leq \mathrm{FR_C} \\ 0.44(\mathrm{FR} - \mathrm{FR_C}) & \text{if } \mathrm{FR_C} < \mathrm{FR} \leq (\mathrm{FR_C} + 1.6) \\ 0.057(\mathrm{FR} - \mathrm{FR_C} - 1.6) + 0.704 & \text{if } (\mathrm{FR_C} + 1.6) < \mathrm{FR} \leq (\mathrm{FR_C} + 6.792) \\ 1 & \text{if } (\mathrm{FR_C} + 6.792) < \mathrm{FR} \end{cases} \tag{2.65}$$

The stripped droplet diameter distribution can be approximated using a model in [10]. The droplets are generated with a random diameter following a Rosin-Rammler distribution:

$$F(D) = 1 - e^{-(D/X)^q} \tag{2.66}$$

where q is a parameter describing the spread of the distribution. X is defined according to:

$$X = \frac{D_d}{(3ln10)^{1/q}} \tag{2.67}$$

D_d is called the parent droplet diameter which is calculated according to:

$$D_d = c_1\frac{\lambda h_{film}}{\pi} \tag{2.68}$$

where c_1 is the droplet diameter scale factor with the value 3.78 according to [10]. The wave length λ is defined as $\lambda = 2\pi/k$ where k_w is the wave number. The wave length used in equation 2.68 is calculated from the most unstable wave number k that corresponds to the maximum wave growth rate. The growth rate, ω, is defined as:

$$\omega = -\left(\frac{\sigma - (\rho_{film} - \rho_c)a/k_w^2}{2\mu_{film}h_{film}}\right)\left(\frac{(k_w h_{film})\sinh(k_w h_{film})\cosh(k_w h_{film}) - k_w^2 h_{film}^2}{\cosh^2(k_w h_{film}) + k_w^2 h_{film}^2}\right) \tag{2.69}$$

where a is the acceleration calculated according to:

$$a = \frac{u_{film}^2 \theta}{h_{film}(\pi + \theta)} \tag{2.70}$$

As with the wave stripping model the edge stripping model is a bit modified when used together with the DMP model. The droplet diameter is not calculated as the stripping occurs, but are selected with the phase setting.

3 Methodology

In this section, the methodology is presented. First, the simplified geometry, that was used for most of the simulations, is presented. But also a complete air intake is simulated. The method is then divided into Lagrangian Multiphase model and Dispersed Multiphase model. Under each model, the simulation approach and the studies that were performed are explained.

3.1 Geometry

The geometry of the air intake is relatively complex. Therefore, a simplified geometry was used. By using a smaller and simpler domain, computational time could be reduced. Furthermore, the simplified geometry could easily be 3D-printed and used for experiments. The simplified air intake consists of the following parts; inlet hemisphere, housing, filter and outlet box, and the boundaries; inlet boundary and fan suction boundary which can all be seen in Figure 3.1.

The new simplified geometry was generated from an existing 3D-cad file of the complete air intake and modified with the CAE pre-processing tool ANSA. The housing, filter and outlet box originate from the complete air intake and were created by taking the cross-section of the complete air intake system and then extruding it in the y-direction. Furthermore, a few smaller geometrical details were removed to get a clean domain. This resulted in a significantly smaller and simpler geometry, but still complex enough to capture the relevant physics, such as impingement, fluid film and stripping. The intake was also widened at the inlet to increase the number of droplets that imping on the inside wall and thereby ease the validation of the impingement and stripping models. The inlet domain was made big and as a hemisphere to avoid reversed flow and to minimize the effect on the flow inside the intake.

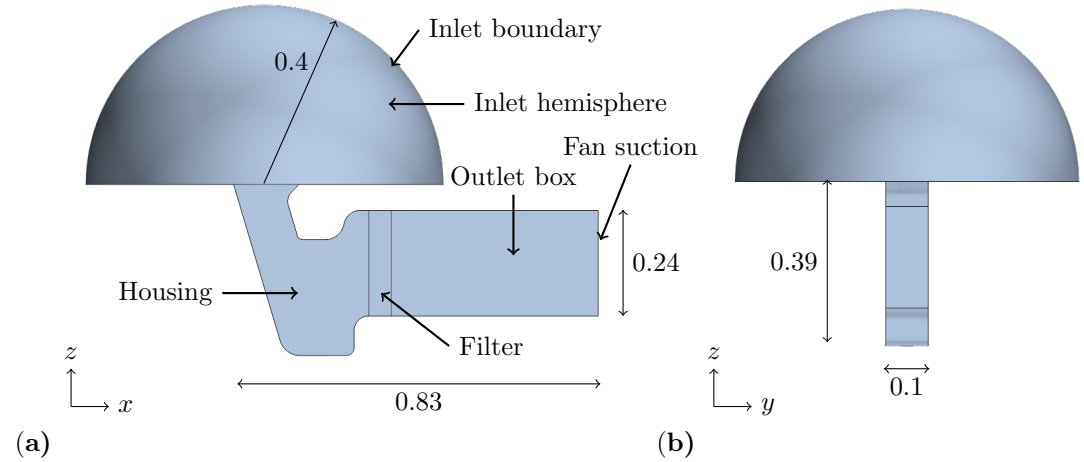

Figure 3.1: Geometry of the simplified domain with the the region names and general dimensions given in meters.

3.2 Lagrangian Multiphase model (LMP)

The Lagrangian Multiphase model was one of the models tested for the dispersed phase in this project. The model is described in Section 2.3 and chosen for its applicability to track the droplets and thereby make it easier to understand the behavior of the droplets in the air intake compared to other models based on the Eulerian approach. It is also less computational expensive compared to DNS multiphase models such as Fluid Film Model.

The automated mesh function in STAR-CCM+ was used to generate the computational grid of the domain. To achieve a conformal mesh between the different parts, the imprint function was used. Thus, a uniform mesh could be created over the interface which resulted in a higher quality mesh.

The surface remesher and automatic surface repair function were used in all four regions. This was to improve the overall quality of the surface mesh and enhance it for the volume mesh. The filter region was modeled as a porous region to resemble the actual filter. In a porous region, the mesh is preferably aligned with the principal flow direction. Therefore, the trimmed cell mesher was used in the filter. In the other three regions, the inlet, the housing and the outlet box, the polyhedral mesher was used. Polyhedral cells have more faces than both the tetrahedral and the trimmed cells. Thus, in general, a higher quality mesh can be achieved with the polyhedral mesh in complex geometries. Furthermore, the volume growth rate was set to 1.2 throughout the whole domain. This to avoid a sudden jump in sizes of neighboring cells. At walls with a no-slip condition, high velocity gradients occurred as explained in Section 2.1.2. To model or resolve these gradients the prism layer mesher was used. To resolve the velocity gradients close to the wall a fine prism layer mesh was needed. To model the velocity gradients with a wall function, a coarser prism layer mesh could be used. However, as a best practice when working with the Fluid Film Model, the thickness of the prism layer cell closest to the wall should be at least twice the thickness of the film thickness [18].

For the continuous phase, a segregated flow model was used together with the assumption of constant density of the gas. The segregated flow model uses a type of Rhie and Chow pressure-velocity coupling together with a type of SIMPLE algorithm [18]. The turbulence model used for the closure of the Reynolds-Averaged Navier-Stokes equations was the Realizable K-Epsilon Two-Layer model which is explained in Section 2.1.1. This model was chosen since it is a good compromise between accuracy, robustness and computational cost. It is also suitable for cases with complex recirculating. A 2nd-order implicit unsteady solver with time step of 1 ms was used for temporal discretization if nothing else is stated. A small study was conducted of temporal discretization and time steps, this is explained in detail in Section 3.2.2.

The fan suction boundary was specified as a velocity outlet. The velocities used during the different simulations were 1.78, 2.66, 3.55 and 4.44 m/s normal to the surface, which is in the positive x-direction. These velocities are scaled using the ratio of the fan suction area of the complete air intake and the simplified air intake to match the corresponding air volume flow rates 50, 75, 100 and 125 liter/s used in the complete air intake. The inlet boundary was specified as a stagnation inlet and all the other surfaces were specified as walls. For the bottom walls of the inlet hemisphere, a slip condition was used for the wall shear stress. This was done to avoid boundary layers to build up at the walls. For the walls of the housing, filter and outlet box, a no-slip boundary condition was used. The boundary condition for the Lagrangian phase was specified to escape for all the walls in the inlet. This means that when the droplets hit any of the walls of the inlet hemisphere they were deleted and removed from the simulation. For all the walls in the housing, the Bai-Gosman model was used to determine the outcome of the droplet impingement. If the droplet passed through the interface between the housing and the filter it was no longer tracked and was removed from the simulation. Furthermore, gravity was applied in the negative z-direction.

The water droplets were tracked with the Lagrangian Multiphase Model (LMP). As explained in Section 2.3, the particles, here droplets, are modeled together as parcels to save computational time. Furthermore, the droplets were modeled as material particles and assumed to have a spherical shape. This assumption is reasonable for droplets with a diameter less than 2 mm as mentioned at the beginning of Chapter 2. To model particle dispersion due to fluctuating fluid forces the turbulent dispersion model was activated.

As stated in the theory chapter, for cases with droplets in airflow, the dominant force exerted on the droplets by the continuous phase is the drag force. Thus, only the drag force was selected and all other particle forces were assumed negligible. The drag coefficient was modeled using the Schiller-Naumann correlation. Due to the small droplets sizes, the Weber number was low, and thus, secondary breakup was not considered.

As explained before, the droplet to wall interaction was modeled with the Bai-Gosman model explained in Section 2.6.1. The model determined which of the outcomes, *adhere*, *rebound*, *spread* or *splash* that would occur and by that indirectly determine if the impinging droplet would create/merge with the fluid film. The walls were treated as dry until the film thickness was larger than zero. The number of secondary parcels produced at the *splash* outcome was set to two with the same reasoning as in 2.6.1, it is a good compromise between cost and accuracy. For calculating the parcel mass ratio r_m as shown in equation 2.37, C_b, C_{rd} and C_{rw} were set to STAR-CCM+'s default values 0.2, 0.6 and 0.75 respectively. The values for C_b and C_{rd} agreed with the values suggested by Bai [1] whereas C_{rw} usually is 0.9. Due to insufficient knowledge about the influence of this parameter, the default value was chosen. For the remaining settings, the suggested values mentioned in the theory were used.

It was important to model the film correctly because stripping droplets from the film may follow the air into the filter. Both the Fluid Film Model, described in Section 2.6.2, and VOF described in Section 2.4 were tested. It was chosen to proceed with the Fluid Film Model for two reasons. To be able to resolve the position

and shape of the interface between the phases when using VOF, the mesh resolution needed to be very high. Thus, this modeling approach was very computationally expensive. The stripped droplets diameter is limited to 25 % of the cell length, or the cubic root of the cell volume. Thus, due to the high resolution of the mesh near the walls, the stripped droplets became unphysically small.

The Fluid Film Model was solved with a segregated flow solver. The film thickness was calculated with equation 2.47 which is the continuity equation, but was also for most simulations limited to maximum 10 mm to avoid divergence problems if film gets stuck in a corner. Similarly was the momentum equation solved with a segregated flow velocity solver. The under-relaxation factors for the film solvers were kept at default values of 0.7. The form drag force model, mentioned in Section 2.6.2 was used to account for the pressure variations from the continuum phase that flows next to the fluid film. Surface tension between the fluid film and the air was taken into account and was assumed to be 0.072 N/m. The material properties were not known. Therefore, the contact angle was assumed to be 90 degrees.

Injectors are used in the LMP model to inject droplets into the domain. The type of injectors can be specified to match the specific case. For all the injectors there are several parameters that can be set. For example, the droplet diameter, the mass flow rate and injection velocity. The droplet diameter can be constant, but can also vary in a specified range. The default injector mass flow rate which was used if nothing else stated was 20 g/s. This resulted in a high volume fraction of water, which is much higher than for natural rain. Due to the high volume fraction of water, two-way coupling was used if nothing else stated. The reason for this mass flow rate was to replicate previously conducted experiments at Volvo Technology's test rig. Furthermore, by injecting water at a high mass flow rate, fluid film was established on the walls of the air intake in a relatively short period of time. The number of parcels that are injected are also specified for the injector by the parcels stream setting, which specifies how many parcels that are injected per injection point and time step. Therefore, when changing the time step, the parcel stream setting also needs to be changed to adjust the number of parcels in the simulation.

Three different injectors were used in this project. The first injector, illustrated in Figure 3.2a, is a part injector that is applied to a presentation grid, located over the inlet to the housing. The grid consists of 400 points that can inject one parcel at each time step. However, the probability that one point injects a parcel is set to 25 percent to get a random distribution of droplets.

The second injector used is a solid cone injector, shown in Figure 3.2b. When performing experiments with the air intakes at Volvo Technology, a cone injector is used to inject water in the incoming air of the air intake. Therefore, this injector is preferred when validating the simulation with an experiment.

The third injector that was used is a part injector that is applied to the whole inlet boundary of the inlet flow domain, shown in Figure 3.3. This injector is more similar to normal rain where the droplets uniformly distributed in the incoming air. This injector has an injection point at each surface cell. A point inclusion probability is set to decide the probability of a point to inject a parcel.

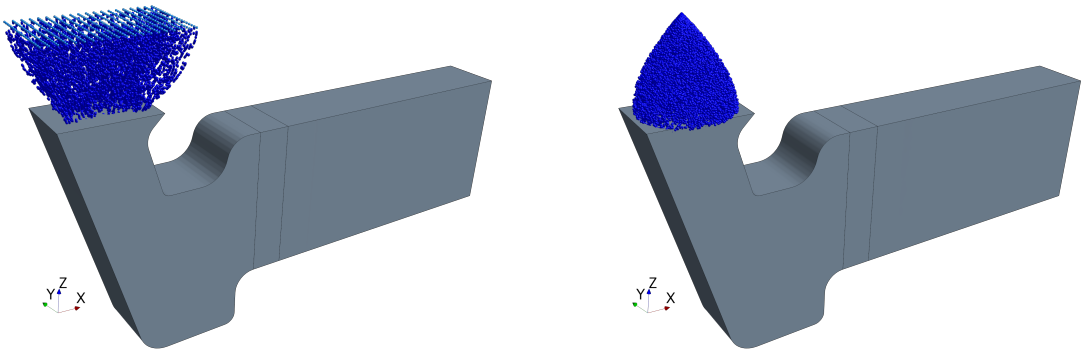

(a) **(b)**

Figure 3.2: a) Injector 1, part injector applied to a presentation grid located above the intake. b) Injector 2, cone injector located above the intake.

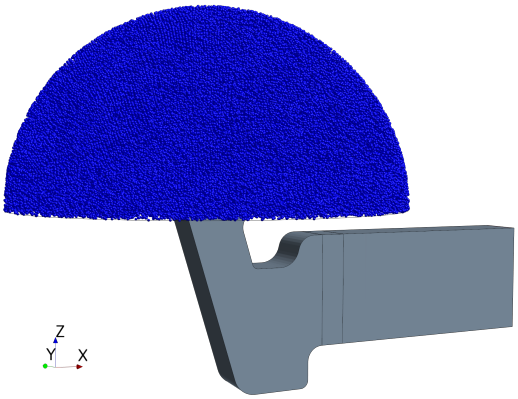

Figure 3.3: Injector 3, the inlet boundary surface used as a part injector.

3.2.1 Mesh independence study

To confirm that the computational grid did not affect the results, a mesh independence study was performed. This study was divided into three different sections, volume cell size, surface cell size and surface cell thickness. Using the results from these three studies a final mesh was selected.

Volume cell size

Four different volume cell sizes were compared to investigate the sensitivity of the volume cell size. These four meshes had the base sizes 7, 8, 10 and 12 mm which was used in the inlet hemisphere. The cell sizes used in the outlet box and housing were 80 % and 40 % of the base size respectively. The cell size in the filter was 2 mm for all meshes. Throughout all the cases the surface mesh size was held constant, both in wall-tangential and wall-normal direction.

Each case was simulated for 2.5 seconds, this was enough time for a significant amount of water to reach the filter. For water injection, the cone injector shown in Figure 3.2b was used. The mass flow rate of water from the cone injector was set to 20 g/s and started after 0.5 seconds. A constant droplet diameter of 0.1 mm was used and the velocity used at the outlet boundary was 1.78 m/s.

A comparison was made of how well the different meshes resolved the air flow. First calculated at time=0.4 s, that is before injection of water, and then at time=2.5 s, which is after injection of water. Two line probes were used to calculate the air velocities. The first line probe was located in the housing close to the inlet and the second line probe was located in the housing close to the filter. Both were located in the middle of the domain in the y-direction. The position of the line probes can be seen in Figure 3.4. Furthermore, the water accumulated in the filter was calculated and compared between the different meshes.

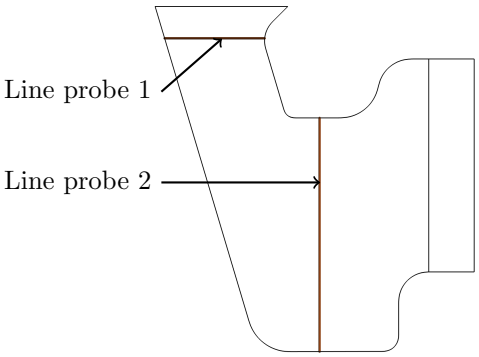

Figure 3.4: Positions of the line probes used for the volume mesh study. Line probe 1 is located in the housing close to the inlet and Line probe 2 is located in the housing close to the filter.

Surface cell size and surface cell thickness

To evaluate how the surface cell size and surface cell thickness affect the impingement, film and stripping, a small domain was used to test the different parameters. The small domain had similar geometry as the simplified domain but was more simplified and of smaller size. The domain with the cone injector used in this study can be seen in Figure 3.5. The behavior of the impingement, film velocity and stripping was measured as the mesh size was changed.

When evaluating the surface cell size thickness the fan suction boundary was used as a velocity outlet with a velocity of 1.74 m/s. The inlet boundary was used as a stagnation inlet. This is the same boundary condition used for most of the studies with the simplified air intake domain. The injector was set to have a mass flow rate of 1 g/s. Two different cell heights were tested, the first one with an approximated cell height twice the film thickness, 0.4 mm, labeled as $1 < y^+ < 5$. This cell height was recommended in STAR-CCM+ tutorial for the film [18]. However, when using this first cell height, y^+ would be in the buffer region ($1 < y^+ < 30$) for some air velocities that were going to be ecamined. The second approach examined was to keep $y^+ < 1$, labeled as $y^+ < 1$. If this was not affecting the film in a negative aspect, this approach is preferred since the boundary layer of the air can then be resolved. Parameters as impingement, film velocity, film thickness and the stripping rate were investigated and compared.

To evaluate how the surface mesh affects the film a different approach was used. All boundaries were set to wall except the inlet boundary that was set to stagnation inlet. Then the water was dropped on the wall with a mass flow rate of 0.03 g/s, showed in Figure 3.5. The film was then flowing down the wall and stripped. The reason for not using any velocity of the air was that when changing the surface mesh the volume mesh also became a bit different because of the maximum cell growth ratios. This may affect how the boundary layer of the moving air is resolved. Therefore, the air was kept stagnated.

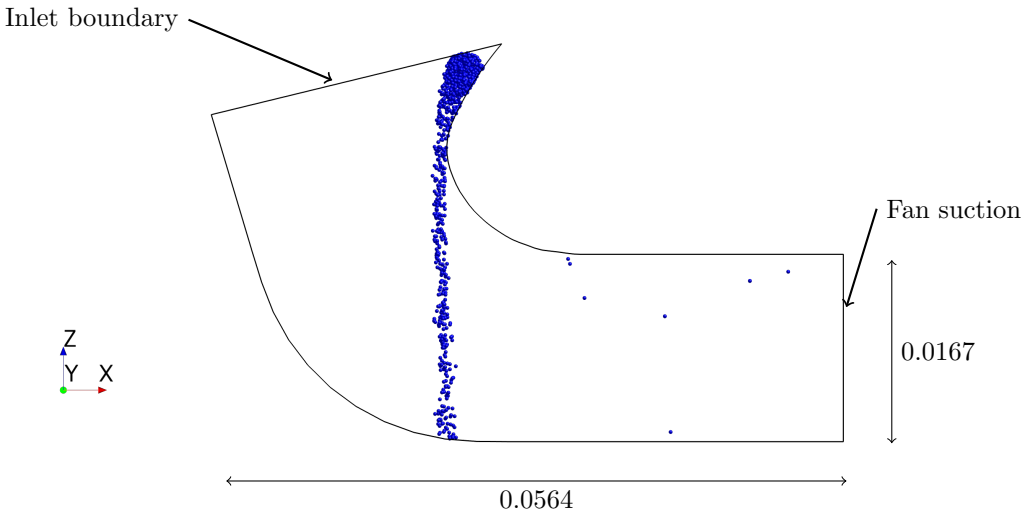

Figure 3.5: The small domain used for impingement and stripping study. The general dimensions are given in meters. At the top of the domain a cone injector is located. The lonely droplets in x-direction have been stripped from the wall above.

3.2.2 Temporal discretization and time step

A comparison between 1st and 2nd order temporal discretization together with various time steps was conducted. Furthermore, two different schemes of tracking integration method were tested, 1st order and 2nd order, where the tracking integration is used to integrate the position and velocity of the droplets. The local time step used in the Lagrangian multiphase solver was determined using Courant numbers. The maximum Courant number which was used as the upper limit for the time step was set to 0.35 and the minimum Courant number which was used as the lower limit for the time step was set to 0.05. All the cases which were examined and compared are listed in Table 3.1.

The study was performed with the simplified air intake geometry and the mass of water in the filter was obtained after 1.8 seconds. The water droplets were injected at 20 g/s mass flow rate using the solid cone

injector shown in Figure 3.2b. A droplets size of 0.05 mm and a air velocity at the fan suction of 1.78 m/s were used.

Table 3.1: All the cases tested and compared with varying temporal discretization, time step and tracking integration method.

Temporal discretization	Time step [ms]	Tracking integration method
1st order	0.05	1st order
1st order	0.1	1st order
1st order	0.5	1st order
1st order	1	1st order
2nd order	0.05	1st order
2nd order	0.1	1st order
2nd order	0.5	1st order
2nd order	1	1st order
2nd order	0.05	2nd order
2nd order	0.1	2nd order
2nd order	0.5	2nd order
2nd order	1	2nd order

3.2.3 One- vs two-way coupling

As explained in Section 2.3, the coupling between the air and the droplets can be one-, two- or four-way coupled. Equation 2.11 was used to calculate volume fraction which varied between the different cases due to the different water mass flow and air flow. None of the cases resulted in a volume fraction of water above 10^{-3}, therefore, the four-way coupling was never considered. For the cases where the fluid film was included, the two-way coupling was used. This is because the two-way coupling is required for the droplets to exchange mass, momentum and energy with the fluid film at the walls.

For the cases where the default mass flow rate of water, 20 g/s, was used, the corresponding volume fractions were in the interval of $1.6 * 10^{-4}$ to $4 * 10^{-4}$ depending on the air volume flow. According to the coupling guidelines given in Section 2.3, the two-way coupling is necessary for this interval. Another mass flow rate of injected water was applied, 0.00375 g/s. This resulted in $3.0 * 10^{-8}$ volume fraction of water for the highest air flow, 4.44 m/s at the fan suction boundary, for which one-way coupling is sufficient according to the guidelines. The reason to examine this was that the volume fraction corresponded to fog/mist as seen in Table 2.2. To investigate the difference between one- and two-way couplings for the two mentioned mass flow rates of water a small study was performed. This is of interest since using one-way is computationally less expensive. For this study, the diameter of the droplet was 0.05 mm which corresponded to the droplet diameter in fog/mist. The droplet was injected using injector 1, shown in Figure 3.2a and an initial velocity of 3 m/s in the negative z-direction. The velocity at the fan suction boundary was 4.44 m/s and the boundary condition at the walls for the droplets was set to escape, thus, no Fluid Film Model for the walls was used.

3.2.4 Parcel convergence study

One of the parameters that was needed to be studied was the number of parcels needed for the simulation to give a statistically converged result. As explained in Section 2.3, the droplets are represented in groups called parcels. More parcels increase the accuracy of the simulation, but also increase the computational time. The number of parcels in the simulations should therefore be as low as possible, but not lower than the point where the solution becomes statistical converged.

For the study of the number of parcels that was needed, the simplified domain was used and simulated several times with different number of parcels. The mass of water accumulated in the filter was the parameter that was calculated and compared. Two droplet diameters were tested, 0.1 mm and 0.05 mm. The droplets were injected after 0.5 seconds with the mass flow rate 20 g/s using the solid cone injector shown in Figure 3.2b. The air velocity at the fan suction boundary was 1.78 m/s and the physical simulation time was set to 1.8 seconds.

3.2.5 Repeatability study

In some circumstances, the mass of water accumulated in the filter could vary a lot for the same case when simulating several times. The reason for this was not known and thus needed to be investigated. The exact same case was simulated several times and the mass of water accumulated in the filter was calculated and compared. Two droplet diameters were tested, 0.05 mm and 0.15 mm. The droplets were injected after 0.5 seconds with the mass flow rate of 20 g/s using the injector shown in Figure 3.2a. The air velocity at the fan suction boundary was 4.44 m/s and the physical simulation time was set to 3 seconds.

3.2.6 Stripping parameter study

When a fluid film breaks up into droplets, it is called stripping. The two models used in STAR-CCM+ to replicate this behavior are called wave stripping and edge stripping, both were tested to conclude which model was needed to capture the physics in the air intake. The edge stripping model is used when the film is driven over a sharp edge as explained in Section 2.6.2. As explained in Section 2.6.2, wave stripping occurs due to body forces and forces from the adjacent fluid flow. Four parameters are used to tune in the wave stripping model to match experimental values. These are C_H, C_H, C_B and the gas velocity scaling factor. Several values were examined for each parameter to increase the understanding of how the parameters affect the stripping. For this study 0.15 mm droplets were injected with an initial velocity of 3 m/s in the negative direction from the injector shown in Figure 3.2a. The mass flow rate of the injected droplets was set to 20 g/s.

These values were used since they resulted in that film was created on the walls fast and thus stripping occurred in a short period of time. To investigate if any of the stripped droplets entered the filter the highest air velocity was used, 4.44 m/s at the fan suction boundary. Higher velocity of the air results in a larger risk that the droplets enter the filter.

3.2.7 Parameter study

In the parameter study, different parameters were investigated to calculate how they affect the results. It is for example of importance to know how the droplet size affects how much water is accumulated in the filter. By knowing this it is possible to see which droplet sizes are critical for the air intake and then use this information when making experiments and designing the air intake. The simplified domain was tested with several droplet diameters. The droplet diameter examined was limited to small droplets compared to normal rain, see the beginning of Chapter 2. This is motivated by that a large droplet diameter will result in a higher Stokes number and therefore the droplets will not follow the air to the same extent. How the velocity of the air affects the droplets was also investigated to see if an increased air velocity increases the amount of water that follows the air into the filter. Finally, three different mass flow rates of water were tested and compared to investigate whether this affects the accumulation of water in the filter. The velocities, droplet sizes and water mass flow rates that were investigated are tabulated in Table 3.2.

The injector that was used in this parameter study was injector type one shown in Figure 3.2a. This injector injected droplets over the inlet to replicate rain, but simplified and less computationally expensive than injector type 3, since the parcels are tracked for a shorter time. The droplets were injected with a velocity of 3 m/s in the negative z-direction.

3.2.8 Simulation of complete air intake system

The complete 3D-geometry of the air intake was based on an existing 3D-CAD of a heavy duty truck climate control air intake system. The CAD file was cleaned with the CAE pre-processing tool ANSA before imported to STAR-CCM+. Compared to the simplified geometry, this geometry is larger and more complex. The complete air intake was simulated with the same boundary conditions as the simplified domain. As for previous simulations the truck is assumed to have zero velocity and the aerodynamics around the truck is not taken into consideration. A moving truck would have a different pressure at the air intake and therefore a different flow through the intake.

Due to confidentiality, an image of the 3D-geometry of this complete air intake system can not be included in this report. The geometry also included a grille which is located between the inlet hemisphere and the housing. The model was simulated with the grille as well as without it. The grille was assigned as a fluid film region when included in the simulation. This was done to capture the physics that happens when the droplets collide with the grille. When small droplets collide with the grille they follow the grille to the bottom of the

Table 3.2: Droplet diameter, air velocity and injected water mass combinations tested for the simplified air intake.

Droplet diameter [mm]	Air velocity [m/s]	Injected water [g/s]
0.01	1.78	20
0.01	2.66	20
0.01	3.55	20
0.01	4.44	20
0.01	4.44	0.00375
0.05	1.78	20
0.05	2.66	20
0.05	3.55	20
0.05	4.44	20
0.05	4.44	10
0.05	4.44	0.00375
0.1	1.78	20
0.1	2.66	20
0.1	3.55	20
0.1	4.44	20
0.1	4.44	0.00375
0.15	1.78	20
0.15	2.66	20
0.15	3.55	20
0.15	4.44	20
0.15	4.44	0.00375
0.2	4.44	0.00375

grille and are then stripped. The new stripped droplets are much larger than the original droplets and therefore they behave differently in the air intake. However, the grille geometry is complex and therefore the effects are difficult to model.

When meshing the 3D geometry the conclusions that were achieved from the study of the simplified domain were used. The meshing strategy that was used before was assumed to be accurate for the 3D-geometry as well. The same surface mesh size of 1.5 mm was used for the fluid film region on the grille as has been used on previous fluid film regions. A prism layer was also added to the grille to keep $y^+ < 1$. This resulted in 5.83 million cells for the whole domain.

The parcel study that was conducted with the simplified geometry was repeated with the 3D-geometry to ensure that the number of parcels needed was not changed.

A study was conducted to investigate if the stripped droplets followed the air into the filter. When setting up this case, photographs and videos of an old experiment conducted at Volvo with the same air intake were used. By visual inspection, from where the droplets were stripped, the size of the droplets and the rate of the stripping could be approximated. Unfortunately, the path of the droplets could not be seen in the video or the pictures. Since the locations from where the droplets were stripped were known, a part injector was used with a line probe as input part, located at the top of the housing relative close to the filter. Using a part injector means that neither the Fluid Film Model nor the stripping models were necessary and computational time could be drastically decreased. The mass flow rate of water was 0.1 g/s and the droplets were injected with zero velocity after 0.5 seconds. Using the approximated droplet diameter from the old experiment and the result of the stripping study conducted on the simplified geometry a normal distribution of droplet diameters was used. The mean value was set to 4.5 mm and the maximum and minimum diameter were 1 mm and 8 mm respectively. Furthermore, the highest velocity of the air used in the air intake was used, which is 4.44 m/s at the outlet boundary.

The parameter study with different particle diameters and air velocities conducted with the simplified domain was repeated with the complete air intake. However, fewer velocities and droplet combinations were tested compared to the simplified domain. The tested parameters are tabulated in Table 3.3. The case with an air velocity of 1.78 m/s was only simulated with a droplet diameter of 0.01 mm. The grille was excluded from

the parameter study. For these simulations, injector 1 showed in Figure 3.2a was used.

The same solver settings that were recommended from the studies with the simplified domain were first used. However, due to problems with divergence for some cases, it was decided to run all the complete air intake simulations with a 1st order time discretization solver.

Table 3.3: Droplet diameter, air velocity and injected water mass combinations tested for the complete air intake.

Droplet diameter [mm]	Air velocity [m/s]	Injected water [g/s]
0.01	1.78	20
0.01	4.44	20
0.05	4.44	20
0.1	4.44	20
0.15	4.44	20

3.3 Dispersed Multiphase model (DMP)

The DMP model can be an alternative to the LMP model for simulation of water separation in air intakes. To evaluate if the DMP model is suitable for the task, it was set up with the simplified air intake geometry and compared to the LMP model. As far as possible, the settings used in the LMP model were also used in the DMP model. However, the models are different and some changes were necessary.

It is not possible to inject water with an injector, as it was done in the LMP model. The inlet boundary was therefore set to a stagnation inlet with a specified volume fraction. Different volume fractions were used for different air mass flows to match the simulations from the LMP model. The outlet boundary was set as an outlet with a specified mass flow rate of 0.1256 kg/s of air. This corresponds to an air velocity at the outlet boundary of 4.44 m/s. Turbulent dispersion was neglected since there is no model that is compatible with the DMP model.

The DMP model is only compatible with one droplet diameter per phase. Thus, the DMP model was only simulated with a constant droplet diameter. However, it is possible to include several phases of water with different droplet diameters. This also means that the stripping droplet diameter must be set before the simulation starts and are therefore not calculated as in the LMP model. More information about this can be found in Section 2.6.2. To make it simple, the phase for stripping droplets were set the same as the main droplet phase. Consequently, the diameter of the stripping droplets was the same as the original droplets. This is of course a simplification. The rest of the simulation settings such as turbulence and wall treatment were kept the same as in the LMP model.

As explained in Section 2.5, the DMP model is compatible with both one- and two-way coupling. To compare with the LMP model both one- and two-way simulations were performed. However, when simulating with one-way coupling the Fluid Film Model was not used since it is not feasible with the one-way LMP model. Instead, the droplet phase was set to phase permeable in the housing region, see Figure 3.1. This was done to be able to compare the simulation with the LMP model.

Two different volume fractions were used, $1.6 * 10^{-4}$ and $3 * 10^{-8}$, which corresponds to the mass flow of water of 20 g/s and 0.00375 g/s. A droplet diameter of 0.05 mm was chosen since previous studies showed that this droplet size will result in a mix of droplets that are separated in the housing and droplets that are entering the filter. Thus, this was the most interesting droplet diameter to simulate.

Due to the complexity of the interaction between phases the convergence can be an issue with the DMP model. To minimize the convergence issues, low under-relaxations factors were used with a ramping function and a time step of 0.1 ms. To stabilize the solver even more, a 1st order convection scheme and temporal discretization scheme were used, but also a 2nd order convection scheme was tested.

In the beginning, it was assumed that the optimal mesh for the LMP model was fine enough for the DMP model as well. Thus, the same mesh was used for all the simulations with DMP. However, later in the project, a mesh study was performed to be sure that the mesh worked with the DMP model. The same approach as the one used for the mesh independence study for the LMP model was used for the DMP model. Four different base sizes were tested and evaluated. For the mesh study, a droplet size of 0.05 mm and an air velocity of 4.44 m/s was used at the outlet. The simulation was one-way coupled and a low volume fraction of $3 * 10^{-}8$ was used. Furthermore, the droplet phase was set to be phase permeable into the housing walls as before.

4 Results and Discussion

In this section, the results of the studies are presented. The structure from the methodology chapter is kept. In the first part, the results from the Lagrangian Multiphase model are presented and in the second part, the results from the Dispersed Multiphase model are presented and compared with the LMP model. Each part is divided into sections for every study that was conducted.

4.1 Lagrangian Multiphase Model (LMP)

Multiple studies about the Lagrangian Multiphase model was explained in Section 3.2. The results of these are presented in this chapter.

4.1.1 Volume cell size sensitivity

The velocity of the air flow at line probe 1 is illustrated in Figure 4.1. The plots represent the air velocity in the negative z-direction at time 0.4 s, thus, before injection of water, and at time 2.5 s, which is after injection of water. Figure 4.2 illustrates the air velocity profile in x-direction for line probe 2 at time 0.4 s and 2.5 s respectively, for the different meshes. As seen for both locations, all the meshes resulted in similar velocities when there were no droplets in the domain. However, once the droplets had been injected into the domain and influenced the air flow, there were some diverging results. The two finer meshes with 7 mm respectively 8 mm base size produced similar results whereas the coarser meshes diverged. The same trend can also be seen in Figure 4.3, where the accumulated mass of water is plotted with respect to time for all the meshes. The two meshes with smaller base sizes resulted in slightly more water accumulated in the filter.

The conclusion of this study is that both the meshes with 7 mm and 8 mm base size are reasonable meshes. The difference in the mass of the accumulated water in the filter was less than 1.6 % between the two. To save computational costs, the mesh with the base size 8 mm was used further on.

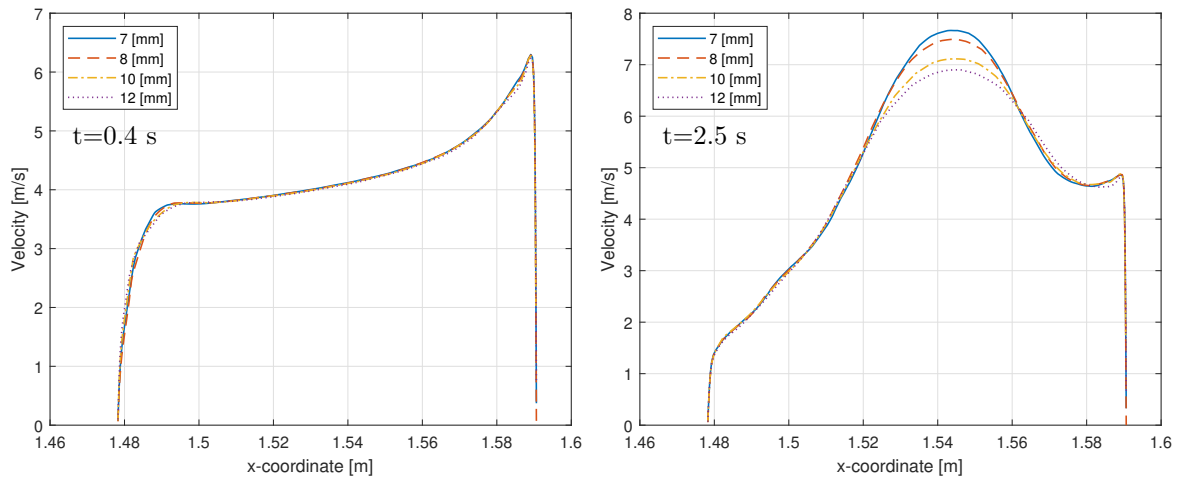

(a) (b)

Figure 4.1: The velocity of the air in the negative z-direction with respect to x-coordinate in the housing for varying volume mesh sizes a) at time 0.4 s (before droplets were injected) b) at time 2.5 s (after droplets were injected).

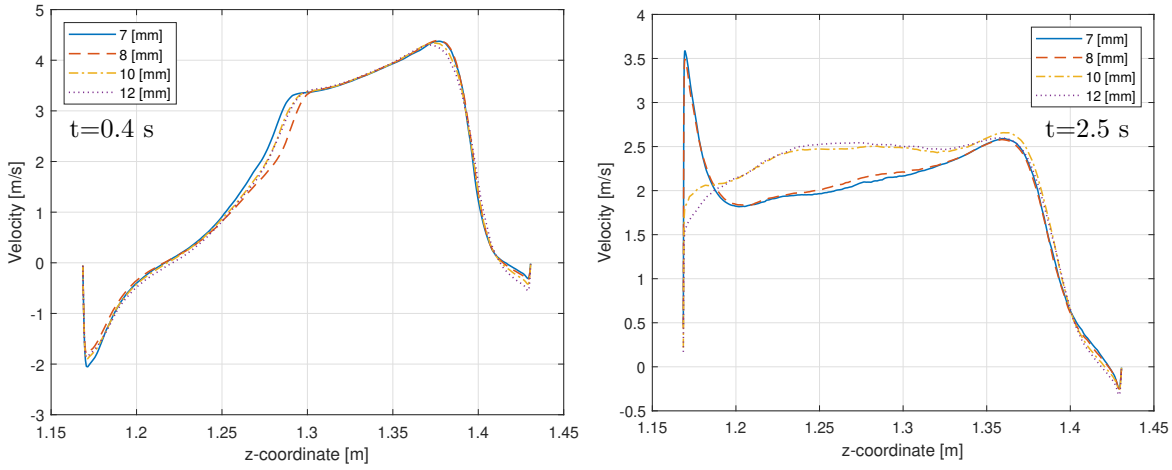

(a) (b)

Figure 4.2: The velocity of the air in the x-direction with respect to z-coordinate in the housing for varying volume mesh sizes a) at time 0.4 s (before droplets were injected) b) at time 2.5 s (after droplets were injected).

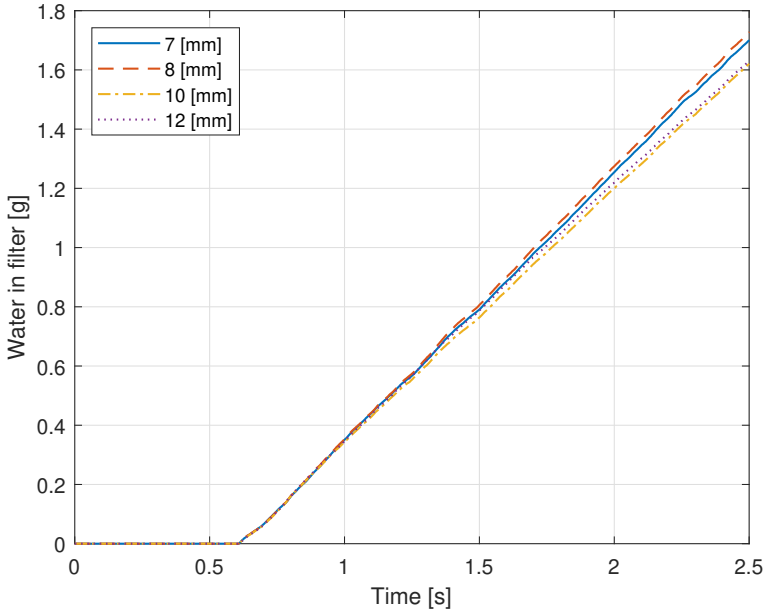

Figure 4.3: Mass of water accumulated in filter with respect to time for varying volume mesh sizes.

4.1.2 Surface cell size

Four different cell sizes were tested, using the small domain illustrated in Figure 3.5, to evaluate how the surface cell size affects the impingement, film behavior and stripping. The data from the simulations are plotted in Figure 4.4 and 4.5. The averaged film thickness and film velocity were independent of the mesh size until stripping occurred. Thus, the impingement seems to be independent of the surface cell size. However, the stripping was varying with the surface mesh size, both regarding when the stripping started and the rate of the stripping. Smaller cell size result in a earlier and more continuous stripping compared to larger surface mesh.

In Figure 4.4b, the maximum film thickness is plotted. As seen in the figure, the maximum film thickness increased with a decreasing surface cell size. This is explained by the fact that the film will become thicker if a parcel impinges on a small cell compared to a large cell. As seen in Figure 4.4b, the film thickness can become unphysically high for small surface cell sizes. This can cause divergence problems. The surface cell size which results in this unphysically film thickness depends on the amount of water that impinges on the wall and the number of parcels used to track the droplets. Unphysical thick film thickness could also occur in corners where

the fluid film cannot escape. To avoid this problem the maximum film thickness parameter in STAR-CCM+ was set to 10 mm for the coming simulations. When the film thickness gets larger than 10 mm, the extra film is removed and lost from the simulation. Thus, mass conservation is not explicitly satisfied.

The optimal surface cell size in a fluid film perspective depends on the case. This study helped to understand which parameters that were needed to be checked, but it is impossible to tell directly from this study what surface mesh that is preferred for the film in the other simulations with the simplified domain. However, a 1.5 mm cell size was used further on.

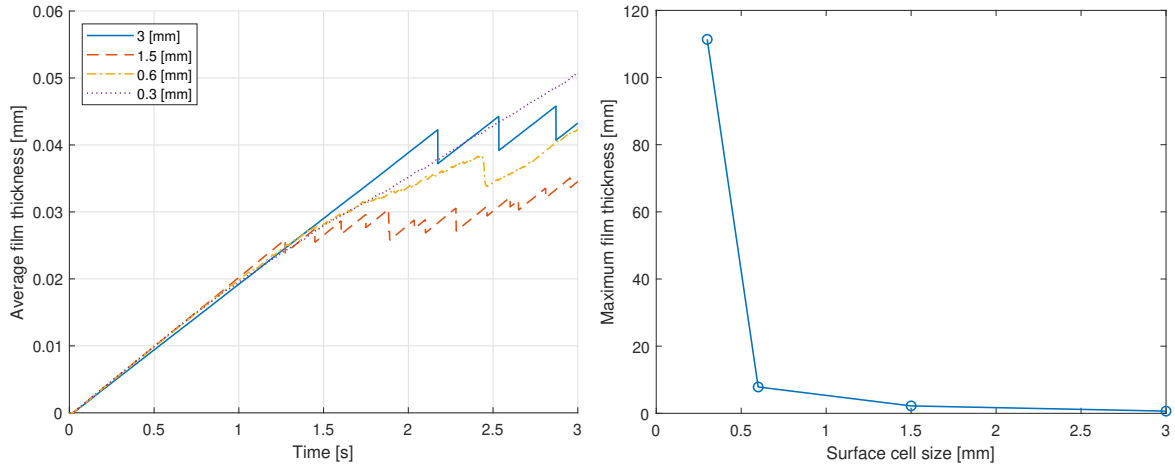

(a) **(b)**

Figure 4.4: a) Average film thickness relative to time. b) Maximum film thickness relative to surface cell size.

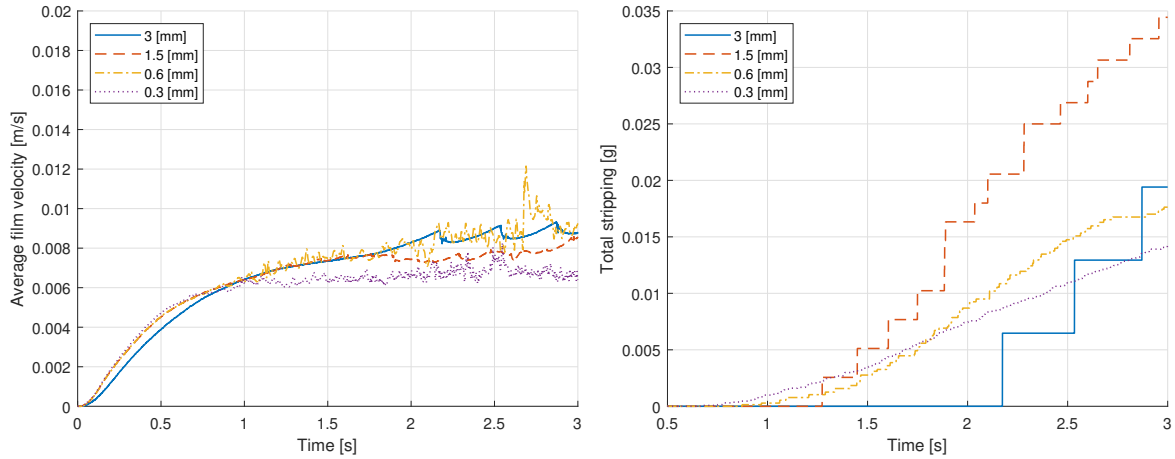

(a) **(b)**

Figure 4.5: a) Average film velocity relative to time. b) Total stripping relative to time.

4.1.3 Surface cell thickness

To evaluate which approach for the surface cell thickness was the best, a study was conducted. As mentioned in Section 3.2.1, the difference between the two tested meshes is the thickness of the first cell at the walls. For $1 < y+ < 5$, the first cell thickness is twice the film average thickness. The second case, $y+ < 1$, had a first cell thickness much lower than the fluid film thickness. In Figure 4.6a the average film velocity and in Figure 4.6b the average film thickness are plotted. The total amount of water stripped from the film are plotted in Figure 4.7. As seen in the figures the results for the two meshes are almost identical. Therefore, it can be concluded that if the first cell thickness is much lower than the film thickness it will have no effect on the film in this case. A mesh strategy with $y+ < 1$ was chosen and the problem to have a y^+ in the buffer region was avoided.

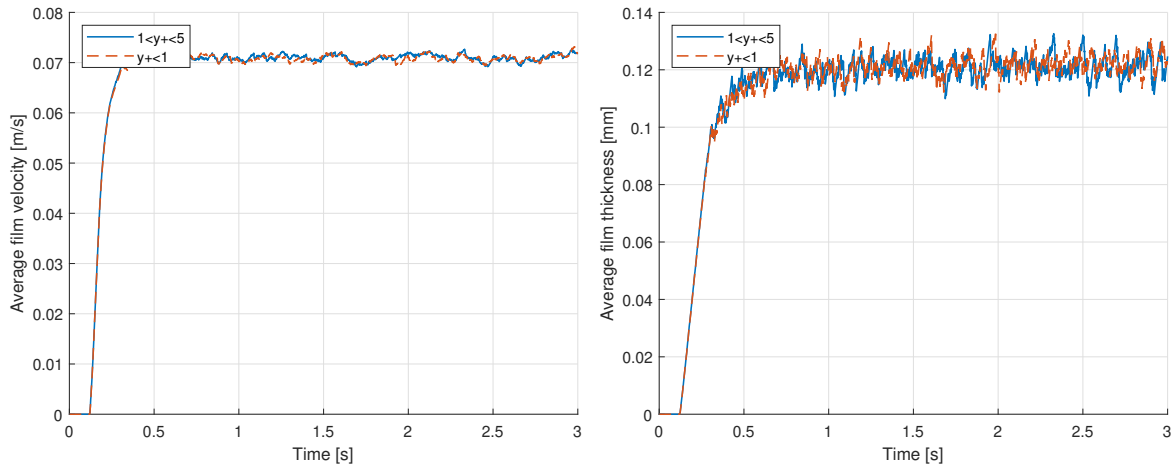

(a) **(b)**

Figure 4.6: Comparison between two surface cell thicknesses. One correspond to y+ between 1.0 to 5.0 and the other correspond to y+ below 1.0. a) Averaged film velocity b) averaged film thickness.

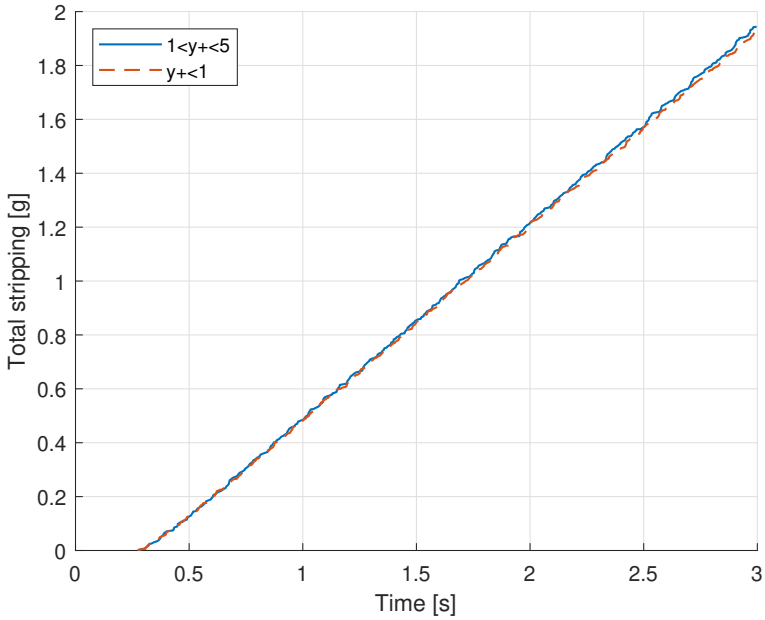

Figure 4.7: Total stripping with respect to time for the two examined surface cell thicknesses. One correspond to y+ between 1.0 to 5.0 and the other correspond to y+ below 1.0.

4.1.4 Final mesh of the simplified domain

From the results of the studies of volume cell size, surface cell size and surface cell thickness, the final mesh was established. Using the base size of 8 mm, surface cell size of 1.5 mm, surface cell thickness of 0.03 mm for the first boundary cell in housing, together with the meshing strategy explained in Section 3.2, resulted in 2.68 million cells. The final mesh is illustrated in figure 4.8, where a) shows the whole domain and b) is a zoomed view at the interface between the inlet hemisphere and housing showing the prism layer in the housing.

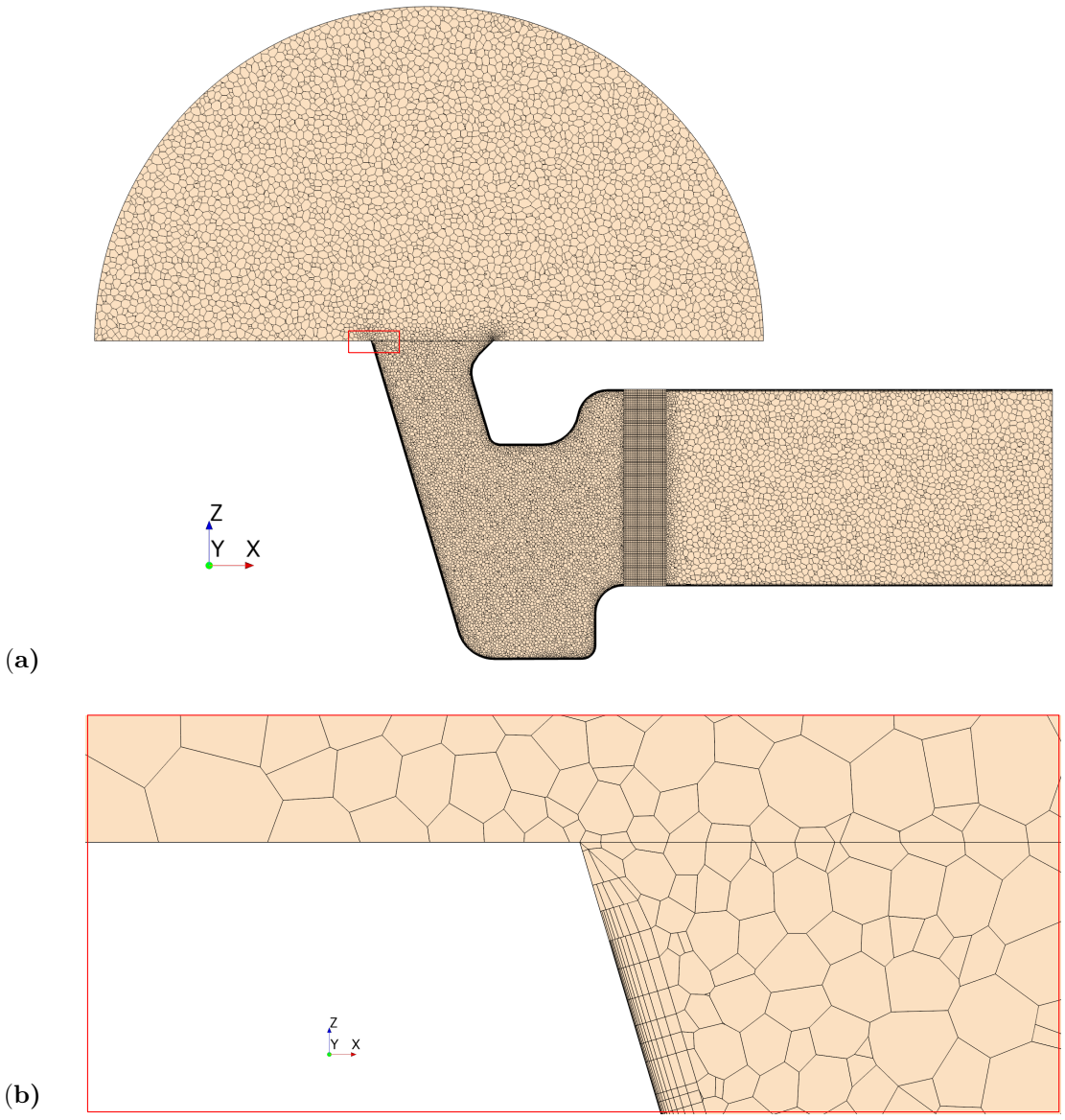

(a)

(b)

Figure 4.8: Cross-sectional view of the final mesh of the simplified domain. a) Whole domain b) zoomed view showing the interface between the inlet hemisphere and housing together with the prism layer in the housing.

4.1.5 Time step sensitivity

A time step study was performed to evaluate how the time step was affecting the results. Furthermore, two different orders of temporal discretizations and two different schemes of tracking integration method for the particles were tested. The study was performed with the simplified air intake geometry and the mass of water in the filter was measured after 1.8 s. All data are plotted in Figure 4.9 and 4.10.

The time step sensitivity study showed that for a first-order temporal discretization a time step of 0.1 ms was small enough for a good convergence. A larger time step will lead to less accuracy even if enough inner iterations are allowed. A time step of 0.5 ms gave an error of 3.37 % while 1 ms resulted in an error of 5 % relative to the smallest tested time step of 0.05 ms.

If a 2nd-order discretization scheme is used, in contrast to the 1st-order scheme, a larger time step can be used. This can clearly be seen in Figure 4.9b were all cases show similar results except the two largest time steps of the first-order temporal discretization scheme.

A higher-order tracking integration method for the Lagrangian droplets, as seen in Figure 4.10, does not influence the result. The default tracking integration method is 1st-order. The 2nd-order is labeled TIM in the figures. A higher-order tracking integration method may allow for a higher Courant number for the droplets. To be sure that it does not influence the result another study needs to be conducted. Using these results, the 2nd-order time discretization with time step of 1 ms and the 1st-order tracking integration method was chosen to use for the following simulations.

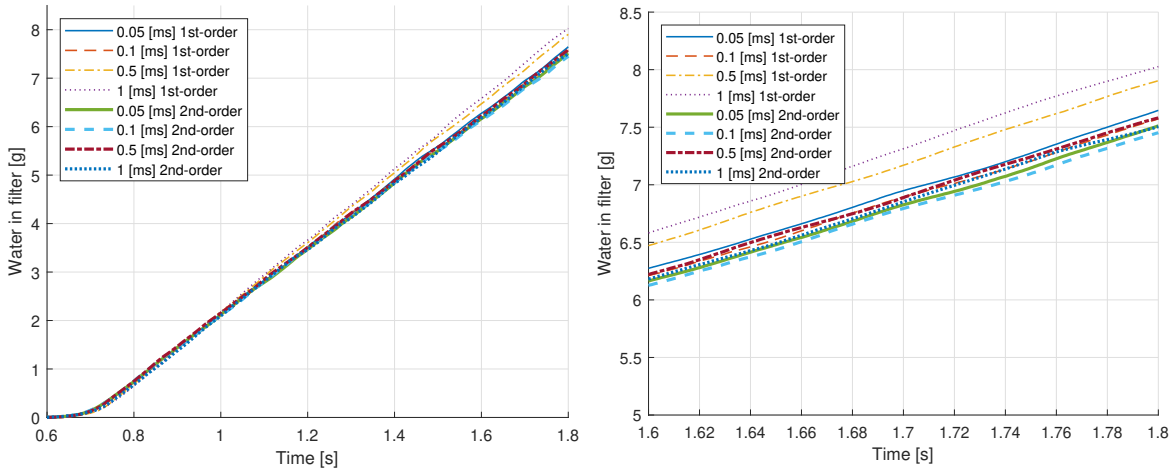

Figure 4.9: Mass of water accumulated in filter with varying time step and temporal discretization a) overview b) zoomed.

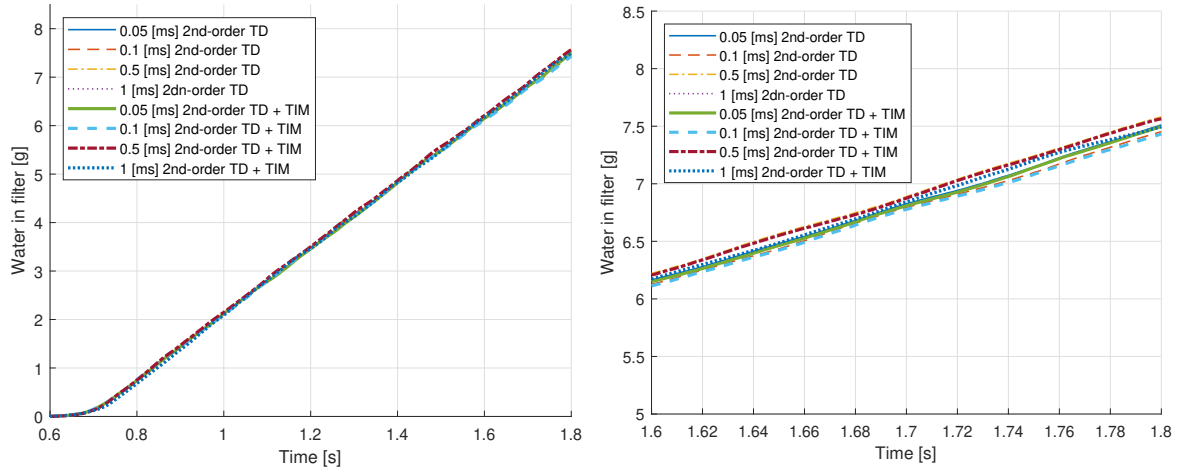

Figure 4.10: Mass of water accumulated in filter with varying time step and tracking integration method a) overview b) zoomed (TD = temporal discretization, TIM = tracking integration method).

4.1.6 One- vs two-way coupling

The case explained in Section 3.2.3 was simulated with two different volume fractions and with one- and two-way coupling. Data from the simulations are tabulated in Table 4.1. As can be seen in the table the difference between one- and two-way coupling was highly dependent on the mass flow rate of the injected water. Injecting 20 g/s of water with the velocity 4.44 m/s at the fan suction boundary resulted in a volume fraction of water around $1.6 * 10^{-4}$. The two-way coupling resulted in 5.24 % water in filter compared to 39.07 % for the one-way coupling. The water percentage in the filter is calculated as the mass of water accumulated in the filter divided by the mass of water entering the housing. The difference is due to the high volume fraction of water. The water affects the air to the extent it has to be accounted for. According to the guidelines of coupling mentioned in Section 2.3, one-way coupling is not sufficient. Therefore, two-way coupling should be used. The effects of the coupling on the droplet trajectories can be seen in Figure 4.11 where a) represents the droplet tracks with two-way coupling whereas b) represents the droplet tracks with one-way coupling. The difference in trajectories of the droplets can be explained using Figures 4.12 and 4.13 which illustrate the velocity field of the air. For the one-way coupled case the recirculation region of air in the bottom of the housing was not affected by the droplets and thus a higher degree of droplets was forced into the filter.

Injecting 0.00375 g/s of water with the velocity 4.44 m/s at the fan suction boundary resulted in a volume fraction of water around $3.0 * 10^{-8}$. For the two-way coupling, 39.27 % of the water that passed through the grille followed the air all the way into the filter, compared to 39.15 % for the one-way coupling. The similarity between the one- and two-way coupling is visualized in Figure 4.14 where a) represents the droplet tracks with two-way coupling whereas b) represents the droplet tracks with one-way coupling. Due to the low volume fraction of water, the droplets do not influence the air to the extent that is had to be accounted for. This can be seen comparing Figure 4.13 and 4.15. The air velocity field is independent of the coupling for such a low volume fraction of water. Thus, when simulating real rain such as fog or mist, one-way coupling is sufficient. However, as mentioned in 3.2.3, the two-way coupling is required for the droplets to exchange mass, momentum and energy with the fluid film. Thus, two-way coupling was used as default for the rest of the simulations.

Represented in Table 4.1 are also the total solver CPU times in seconds for all the cases. When injecting 20 g/s of water the total solver CPU time using two-way coupling was 36.7 times higher than when using one-way coupling. When injecting 0.00375 g/s of water the total solver CPU time using two-way coupling was 3.5 times higher than when using one-way coupling. However, the high performance computing (HPC) cluster used for the different simulations are not known and can differ. Therefore, part of the difference in CPU time can be explained by that a different cluster had been used for the cases.

Table 4.1: Comparison between one- and two-way coupling for two mass flow rates of water.

Coupling	Water from injector [g/s]	Water in filter [%]	Total solver CPU time [s]
Two-way	20	5.24	9.17E+07
One-way	20	39.07	2.50E+06
Two-way	0.00375	39.27	7.67E+06
One-way	0.00375	39.15	2.21E+06

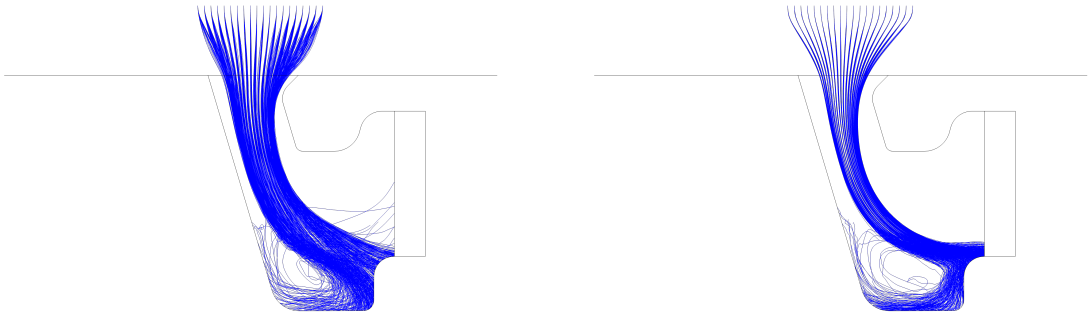

(a) **(b)**

Figure 4.11: Trajectories of the droplets in the housing with 20 g/s of water using a) two-way coupling b) one-way coupling. The droplets are more distributed in the housing using two-way coupling than one-way coupling.

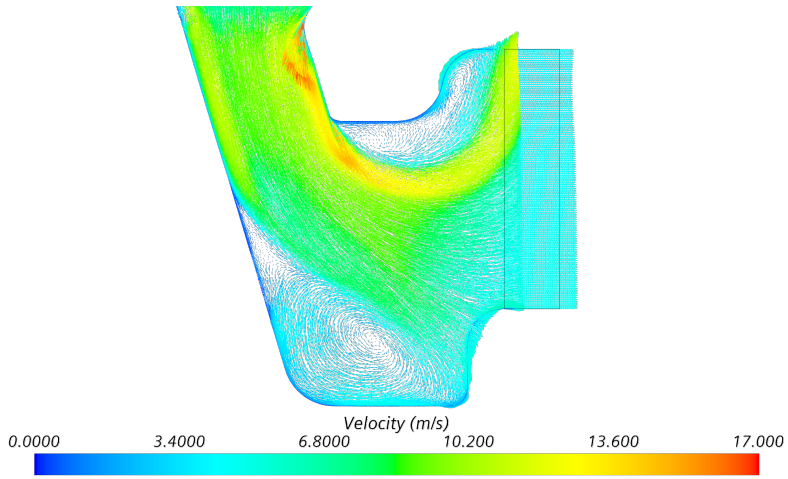

Figure 4.12: Velocity field of the air in the housing with 20 g/s of water at second 3 using the two-way coupling. A small recirculation region of air can be seen in the bottom of the housing.

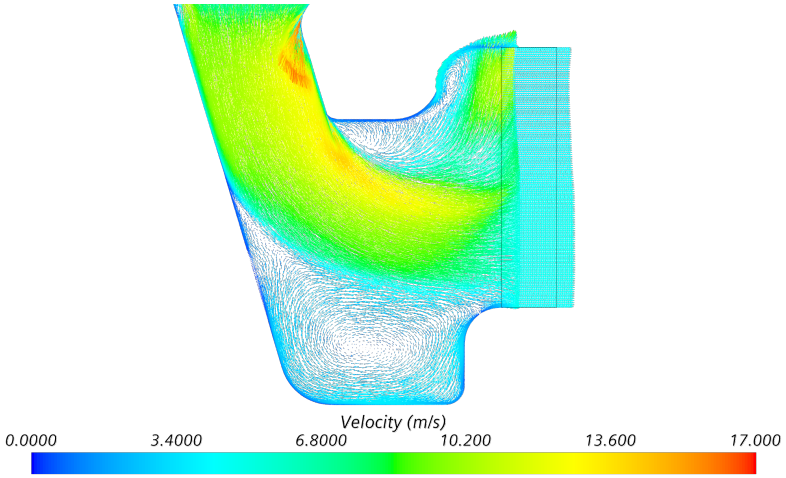

Figure 4.13: Velocity field of the air in the housing with 20 g/s of water at second 3 using the one-way coupling. A larger recirculation region of air can be seen in the bottom of the housing compared to simulation using two-way coupling, see Figure 4.12.

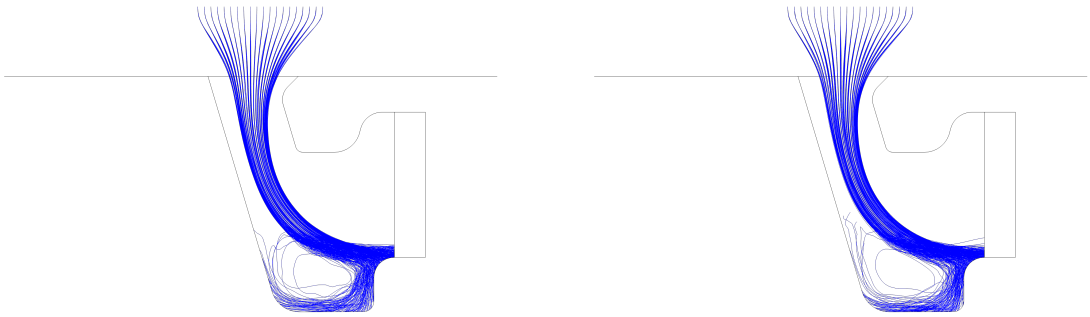

(a) **(b)**

Figure 4.14: Trajectories of the droplets in the housing with 0.00375 g/s of water for a) two-way coupling b) one-way coupling. The similarity of the trajectories depends on the low volume fraction of water.

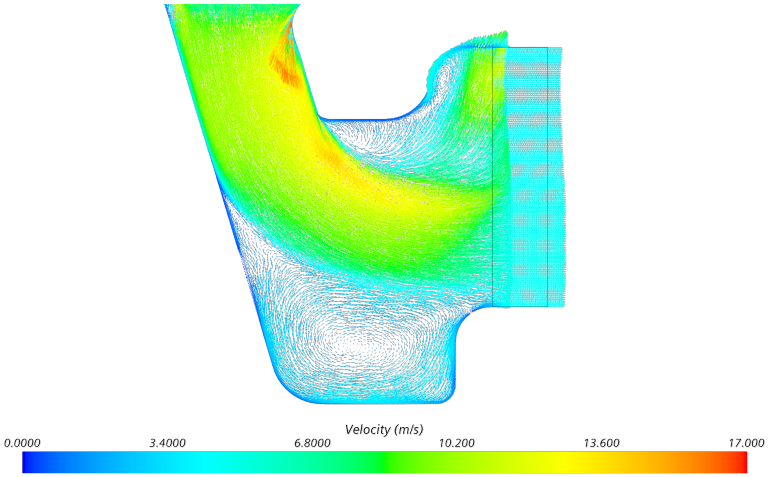

Figure 4.15: Velocity field of the air in the housing with 0.00375 g/s of water at second 3 using the two-way coupling. A recirculation region of air can be seen in the bottom of the housing similar to the simulation with 20 g/s of water using one-way coupling.

4.1.7 Number of parcels sensitivity

The total mass of water accumulated in the filter is the most important parameter. Therefore, this parameter was used when investigating the number of parcels that were needed for a converged result.

In Figure 4.16, the data is plotted for the different number of parcels and two different droplet sizes, 0.05 and 0.1 mm. The data can also be seen in Table 4.2 and 4.3. Both cases with droplets sizes of 0.05 mm and 0.1 mm, started to converge using 500 000 parcels/s. This resulted in an error of 2.81 % and 4.22 % respectively, compared to 700 000 parcels/s. With 500 000 parcels/s and a droplet diameter of 0.05 mm, each parcel consists of 612.65 droplets compared to 76.58 droplets per parcel for a droplet diameter of 0.1 mm. Therefore, in this case, the important parameter is the injection rate of parcels and not the number of droplets per parcel.

The mass flux into the filter for three different cases can be seen in Figure 4.17. When a lower number of parcels is used in the simulation, it does not only result in a lower amount of water in the filter, it also results in a larger spread of the mass flux into the filter.

Since both cases with a droplet diameter of 0.05 and 0.1 mm droplets diameter, converged at 500 000 parcels/s this is the number of parcels that are used as the default in the coming simulations. The reasoning of choosing 500 000 parcels/s was also due to the computational power that was available. If a higher number of parcels would have been used the results had become even more accurate, but with a high cost in terms of computational power. However, if a polydisperse distribution of droplets was used, a higher number of parcels would probably have been needed to get a good resolution of the size distribution.

Table 4.2: Data from parcel stream study, particle size: 0.05 mm.

Parcels/s	Droplets/parcel	Error
100 000	3063.20	33.54 %
200 000	1531.60	16.72 %
300 000	1021.10	9.74 %
400 000	765.81	5.17 %
500 000	612.65	2.81 %
600 000	510.54	0.88 %
700 000	437.61	-

Table 4.3: Data from parcel steam study, particle size: 0.1 mm.

Parcels/s	Droplets/parcel	Error
100 000	382.91	46.29 %
200 000	127.64	14.27 %
500 000	76.58	4.22 %
600 000	63.82	1.95 %
700 000	54.70	-

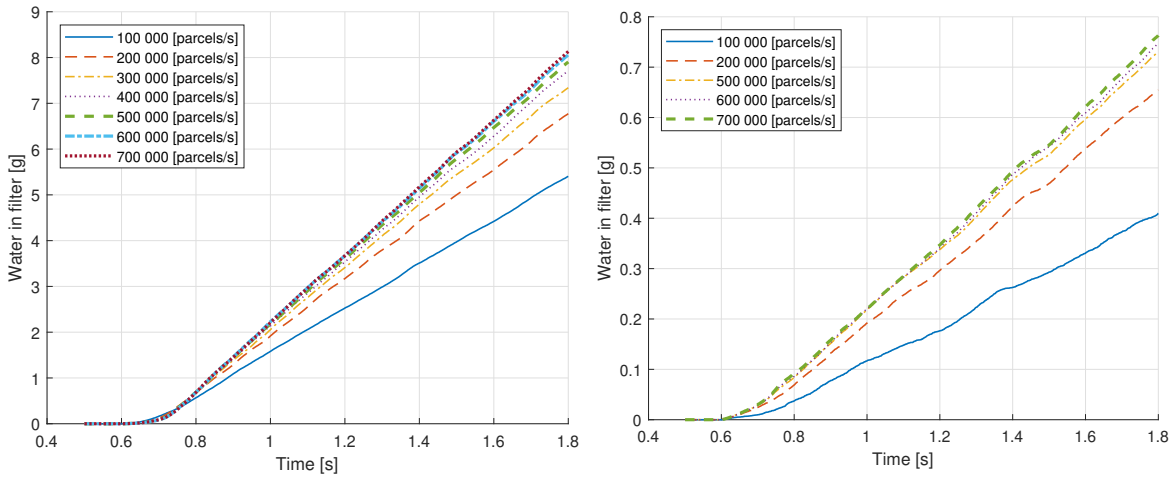

Figure 4.16: Water accumulated in filter with respect to time for simulations with different number of parcels a) droplet size: 0.05 mm b) droplet size: 0.1 mm

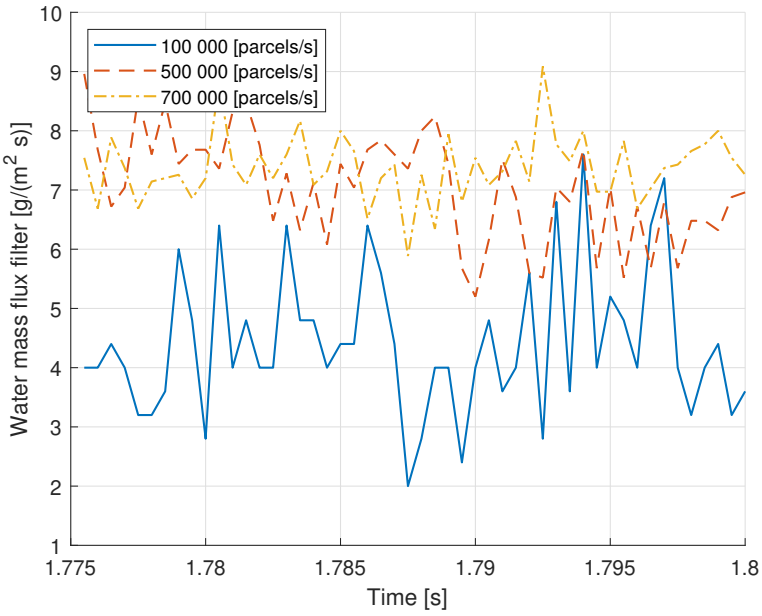

Figure 4.17: Water mass flux into filter relative to time. Notice that the time frame is 0.025 seconds. As seen in the figure, a higher number of parcels result in a lower spread of mass flux.

4.1.8 Repeatability

In some circumstances, the result varied a lot when simulating the same case several times. This can be explained with the multiphase models that were used.

One of the cases with the problem is illustrated in Figure 4.18a. The mass of water accumulated in the filter with respect to time is plotted in Figure 4.18b. As seen, the number of droplets that are transported to the filter varies between the simulations.

In this simulation, the droplets were of the largest diameter, 0.15 mm. The heavy droplet mass made the droplets fall directly to the bottom of the air intake and then transform to film, *rebound* or *splash*. No droplets did flow into the filter without first being in contact with a wall. When *splashing*, the droplets split into several droplets and also transfer some mass to the film. Therefore, the new droplets are smaller than the parent droplet and can be transported to the filter by the air flow. However, as explained in Section 2.6.1, the *splashing* model is based on some random parameters. Both the diameter and the direction of the secondary parcels are random. The turbulent dispersion model is also based on random parameters as explained in Section 2.3.1 and therefore can the trajectories vary for droplets from time to time.

Because of the low number of parcels that were transporting the droplets to the filter the result was not converged. Therefore, a higher number of parcels were needed for the result to be converged. This can be done by increasing the number of parcels or increasing the simulation time. However, the amount of water that reached the filter was so low that it can be negligible. In other cases when more droplets reached the filter this problem did not occur. This could be seen when the five identical simulations using the droplet diameter of 0.05 mm were compared. Due to the larger number of parcels that had hit the filter the results were converged and were the same for all the five simulations.

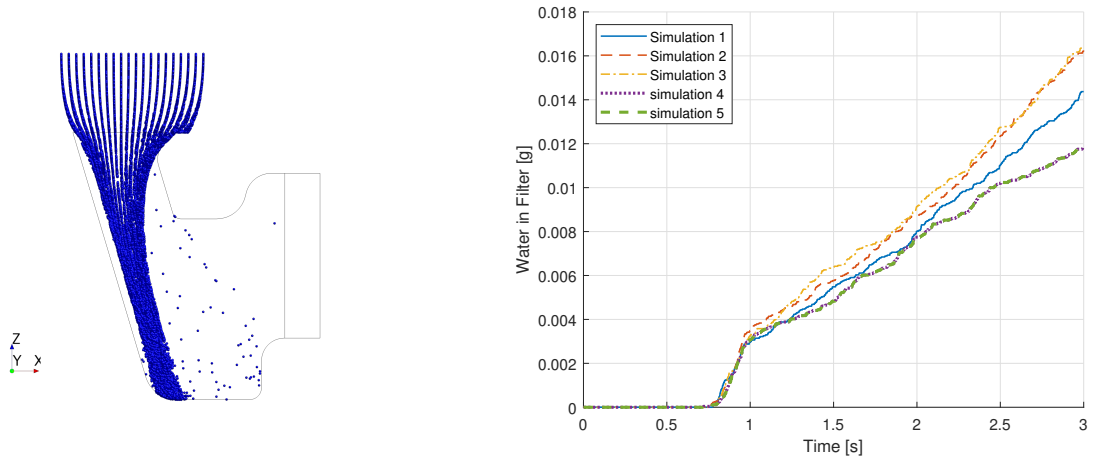

(a) **(b)**

Figure 4.18: The exact same case simulated several times. a) Droplets fall directly to the bottom and *splash*, *rebound* or transform to fluid film. b) Comparison of the accumulated mass of water in the filter.

4.1.9 Stripping parameter study

The results from the study of droplets stripping from the fluid film as explained in Section 3.2.6 are presented here. The injected droplets created a fluid film on the walls. On the wall of interest, which can be seen in center of Figure 4.19, the film flows downwards due to gravity and due to the drag from the air to the curved edge. At this edge, the film was accumulated and stripped into droplets. Only from this wall can the stripped droplets enter the filter.

The edge stripping model did not result in any stripping since there are no sharp edges for the film to be driven over. Thus, this model was not further used and just the wave stripping model was applied. The four parameters used to tune in the wave stripping model were tested and the result is explained below.

The parameter used to control the minimum thickness of the film at which stripping occurs is C_H. Five different values were tested, 0.5, 0.8, 1.0, 1.2 and 1.5 where 1.0 is the default value used in STAR-CCM+. Illustrated in Figure 4.20 is the total amount of stripping in gram during the first three seconds for the five

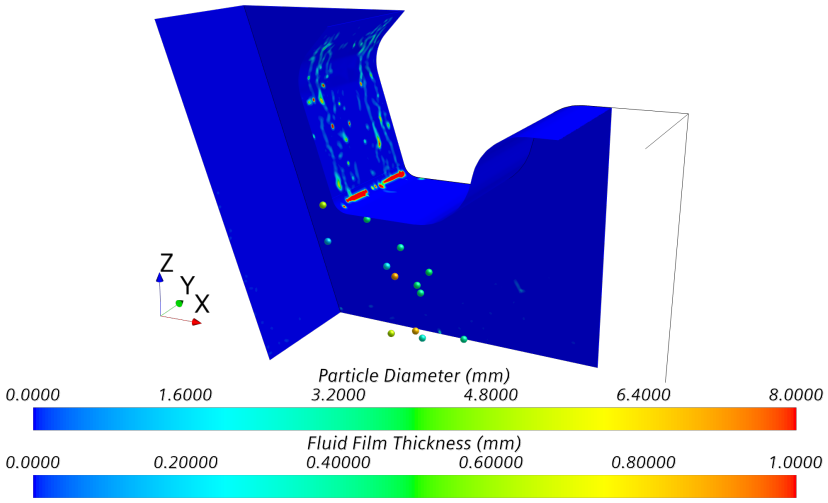

Figure 4.19: Fluid film thickness on the walls of the housing and the stripped droplets diameter in mm after three seconds.

values of C_H. As can be seen, the lower values of C_H result in more stripping and the higher values in less stripping. This is because the minimum film height for stripping to occur is lower for lower C_H, and thus, the stripping occurs earlier.

The parameter C_D is used to control the size of the stripped droplets. Five values were tested to investigate the influence of C_D, 3.0, 3.4, 3.78, 4.2 and 4.6 where 3.78 is the default value. Figure 4.21a shows the average droplet diameter of the stripped droplets. Higher C_D results in larger droplet size and the default value 3.78 results in an average droplet diameter of 3.34 mm. Figure 4.21b represents the total amount of stripping in gram for the same values of C_D. No trend can be seen for the different values and the difference is assumed to be random.

The last two parameters that were tested were C_B, which controls the rate of the stripping and the gas velocity scaling factor. The correlation between these parameters and the total amount of stripping can be seen in Figure 4.22. A trend where higher C_B resulted in more stripping can be seen with the exception of $C_B = 1$. All the values for the gas velocity scaling factor result in a similar amount of stripping except for the value 9.5. The discrepancies are small and assumed to be random.

All these parameters are used to tune in models to match the results of experiments. Due to lack of experimental data the default values of $C_H = 1$, $C_D = 3.78$, $C_B = 1$ and gas velocity scaling factor = 10 were used for all the remaining simulations. Using the default values for wave stripping and the highest volume air flow the stripped droplets did not enter the filter. This can be seen in Figure 4.23 where the trajectories of the droplets which had been stripped are plotted. The trajectories are color-coded with respect to the corresponding droplet diameter. The droplets which have entered the filter in the figure had either *rebounded* or been *splashed* against the wall.

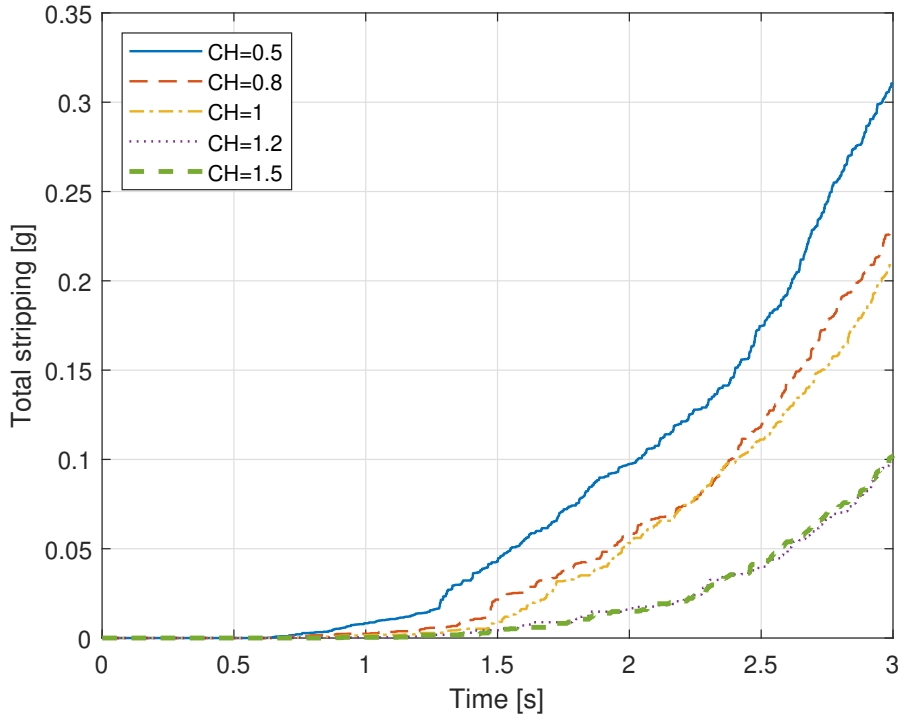

Figure 4.20: The total amount of stripping in the domain measured in gram of water with varying values of C_H. C_H controls the thickness threshold at which stripping occurs.

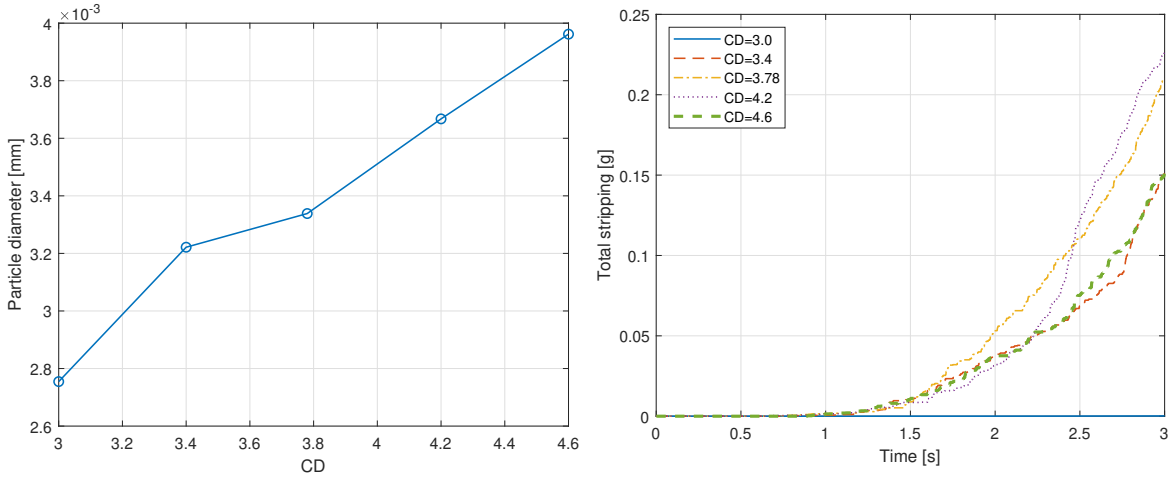

(a) **(b)**

Figure 4.21: A comparison between cases with a varying CD. CD controls the size of the stripped droplet. a) Average droplet diameter in mm of the stripped droplet b) Total amount of stripping in the domain measured in gram.

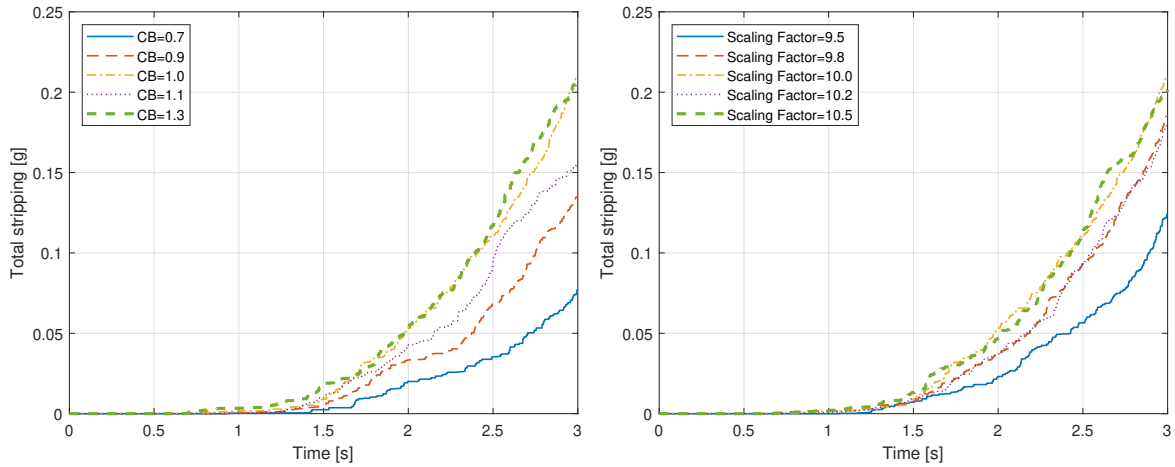

(a) **(b)**

Figure 4.22: The total amount of stripping in the domain measured in gram a) with varying CB which controls the rate at which film mass is stripped b) with varying Gas Velocity Scaling Factor.

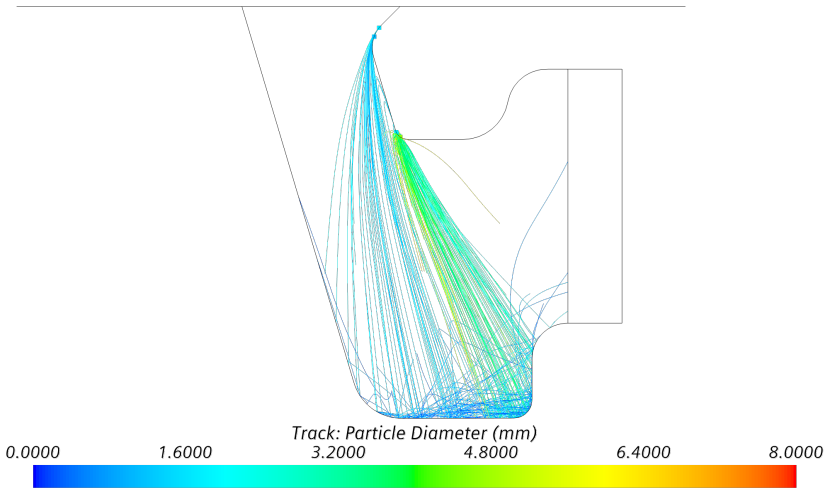

Figure 4.23: Trajectories of the droplets that have been stripped in the housing.

4.1.10 Parameter study

As mentioned in Section 3.2.7, several parameters were tested to examine how these affect the quantity of water accumulated in the filter. Figure 4.24 illustrates the water accumulated in the filter after three seconds for varying droplets diameters and velocities of the air. For all the cases the injected mass flow rate of water was held at a constant rate of 20 g/s. The y-axis displays how high percentage of the incoming water to the housing that is flowing into the filter. This quantity is calculated as the mass of water accumulated in the filter divided by the mass of water entering the housing. As expected, the small droplet diameter resulted in more water in the filter. The smallest droplet diameter tested, 0.01 mm, which corresponds to fog, resulted in the interval 80 to 92 % mass of water in the filter depending on the velocity of the air. Droplet diameter of 0.05, 0.1 and 0.15 mm resulted in the intervals 13-29 %, 0.8-4 % and 0.1-0.7 % respectively. Thus, at the size of the droplets which corresponds to mist, not more than 4 % of the water entered the filter. It is also interesting to observe how the velocity of the air was affecting the quantity of water in the filter. It was found that there was no obvious trend. For the cases with droplet diameter 0.01 mm the higher air velocity resulted in more mass of water in the filter. However, the opposite trend could be seen for a droplet diameter of 0.05 mm. Lower air velocity resulted in more mass of water in the filter.

A small margin of error should be taken into consideration when discussing the percentage of water in the filter. As mentioned before, the percentage of water in the filter is calculated by dividing the accumulated water mass in the filter by the total amount of water mass that entered the housing, both measured at time=3 s. Thus, some of the droplets in the housing, that would enter the filter if given enough time, are not taken into account. Consequently, the percentage is a bit lower than it should be when including the droplets in the housing at time=3 s.

Figure 4.25 illustrates the droplet trajectories in the housing using a) 0.01 mm droplets b) 0.05 mm droplets c) 0.1 mm droplets d) 0.15 mm droplets. All the cases had the same velocity at the fan suction boundary, 4.44 m/s. Using 0.01 mm droplets resulted as shown in the figure that more or less all of the droplets entered the filter. For 0.05 mm droplets, most of the droplets hit the vertical wall in front of the filter and created a fluid film. For the larger droplet diameters of, 0.1 and 0.15 mm, all the droplets hit the bottom horizontal wall of the housing. The few droplets that entered the filter had either *rebounded* or been *splashed*.

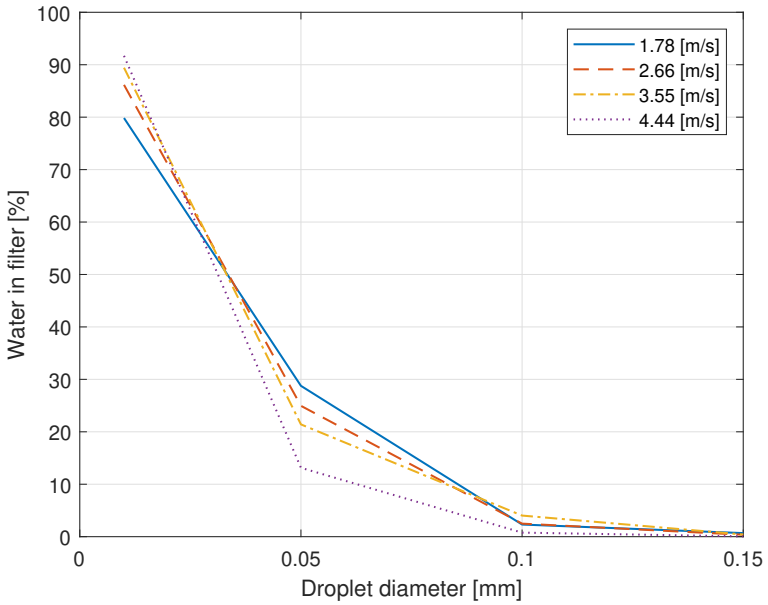

Figure 4.24: Accumulated water in the filter after three seconds for varying droplets diameters and air velocities.

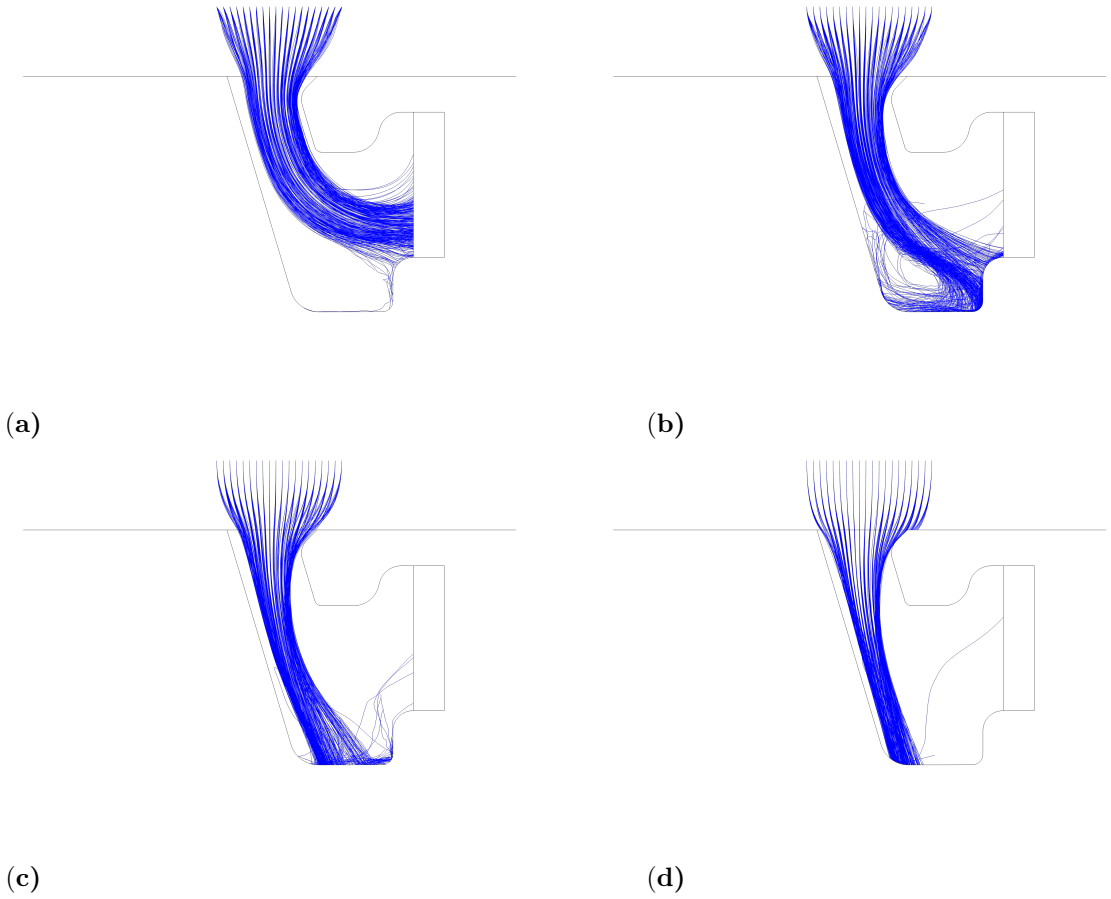

Figure 4.25: Droplet trajectories in the housing with 4.44 m/s at the fan suction boundary, 20 g/s of water injected and using a) 0.01 mm droplets b) 0.05 mm droplets c) 0.1 mm droplets d) 0.15 mm droplets.

The influence of the mass flow rate of water was also investigated. The mass flow rates 0.00375, 10 and 20 g/s of water were tested and compared using constant droplet diameter 0.05 mm and the highest velocity of the air, 4.44 m/s at the fan suction boundary. Given in Table 4.4 are the percentages of water in the filter for the three cases. 20 g/s which correspond to the mass flow rate used in previously performed experiments at Volvo, resulted in 13.14 % water in the filter. Lowering the injected water to 10 g/s marginally increased the percentage of water in the filter to 14.28. However, decreasing the injected water to 0.00375 g/s, which correspond to fog/mist, the percentage of water in the filter became 43.30 %. This difference can also be seen in Figure 4.26 which illustrates the droplet trajectories in the housing with 0.05 mm droplet diameters using two mass flow rates for the injector, a) 20 g/s of water and b) 0.00375 g/s of water. The reason for the differences in water percentage that is flowing to the filter between the low and high water flow rates, for the droplet size of 0.05 mm, is that for the two highest flow rates there is enough water droplets in the domain to influence the air flow. In the case with lower water flow rate, the droplets are not influencing the air flow. The change in airflow for the two highest mass flow rates results in a decreased percentage of the water that is flowing into the filter.

Figure 4.27 illustrates the relations between the droplet diameter, mass flow rate of water and the percentage of water that is flowing into the filter. The percentage of water in the filter is plotted for the water mass flow rates 0.00375 and 20 g/s with varying droplet diameters. The low water mass flow rate resulted in more water in the filter for all the droplet diameters except for 0.1 mm. It is not known why results for 0.1 mm droplet deviate from the other droplet sizes. This needs to be further investigated. One possible explanation might be the fact that the *rebound* outcome of droplet-wall impingement does not occur as frequently as for the other cases. This would explain the deviating result since for droplet diameter of 0.1 mm or larger most of the droplets entering the filter either *rebound* or *splash*.

Table 4.4: The amount of water accumulated in the filter for varying injected water mass flow rates. Droplet diameter=0.05 mm and 4.44 m/s velocity of the air at the outlet boundary.

Injected water [g/s]	Water in filter [%]
0.00375	43.30
10	14.28
20	13.14

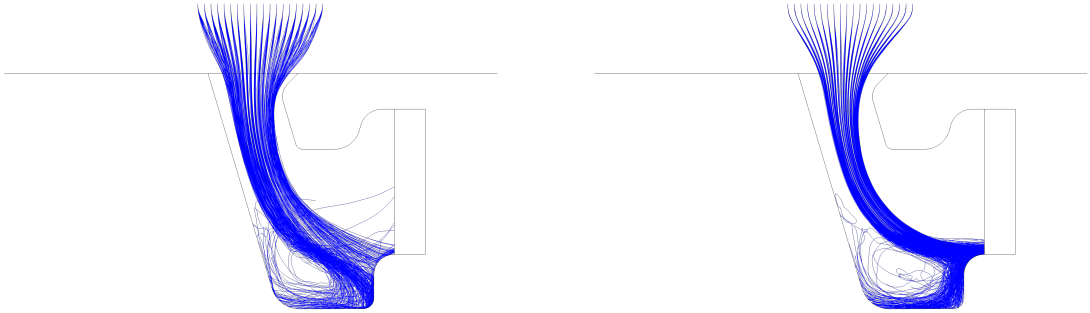

(a) **(b)**

Figure 4.26: Droplet trajectories in the housing with 4.44 m/s at the fan suction boundary and 0.05 mm droplet diameters. a) 20 g/s of water b) 0.00375 g/s of water.

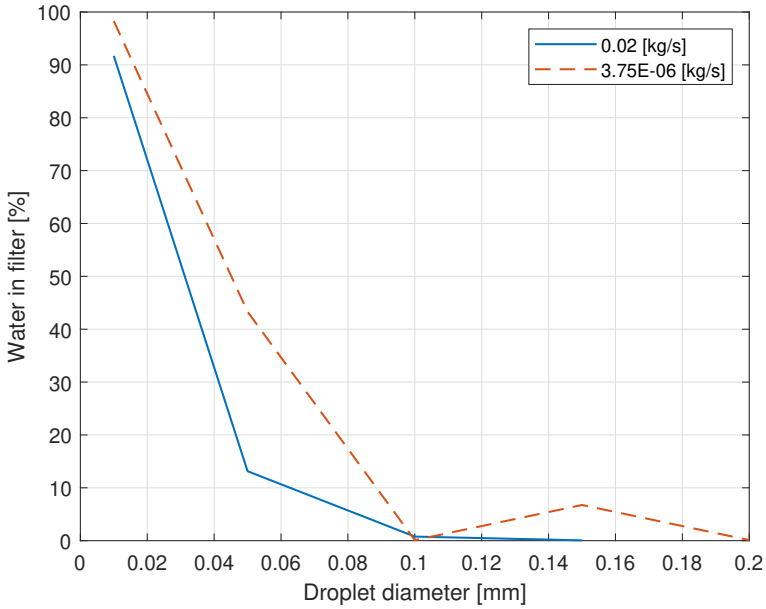

Figure 4.27: Accumulated water in the filter after three seconds for varying droplets diameters and injected mass flow rates of water. 4.44 m/s velocity of the air at the outlet boundary.

4.1.11 Complete air intake simulation

The complete air intake was simulated with the LMP and Fluid Film models in the same manner as the simplified domain. The knowledge gathered from the previous studies was applied to the complete air intake.

The complete air intake geometry is, as explained in the previous chapter, much more complex than the simplified geometry. Therefore, another parcel study was conducted to assure that the number of parcels needed for the simulation to achieve a converged result was not changed. The data from the study is plotted in Figure 4.28. The data showed that the result starts to become constant when the number of parcels reaches about 400 000 parcels/s. This was very close to the result that was achieved from the parcel stream study with the simplified domain. The previous study also showed that the particle diameter does not change the number of parcels needed in a significant way. Therefore, it was decided to use 500 000 parcels/s.

As explained in Section 3.2.8, a case was simulated to investigate if the stripped droplets followed the air into the filter. The result of this study is illustrated in Figure 4.29. The trajectories of each parcel are shown with the color representing the droplet diameter. The larger droplets can be seen falling more or less straight downward whereas the smaller droplets are more affected by the air flow. However, just as for the simplified geometry, none of the droplets entered the filter.

The parameter study was conducted without the grille. The data are plotted in Figure 4.30 and were sampled after a solution time of three seconds. The droplets showed similar behavior as in the simplified domain. This was expected since the geometries are similar. Smaller droplets resulted in more water accumulation in the filter. For the largest droplet size tested, 0.15 mm, almost no droplets followed the air into the filter. For the diameters around 0.05-0.1 mm, 6-12 % of the water that entered the housing followed the air into the filter. This is about the same amount of water that was accumulated in the filter for the simplified domain for the same droplet diameters and air velocities. However, for the smallest droplet tested, 0.01 mm diameter, only 54 % of the water entered the filter, compared to 80 % for the simplified domain. Figure 4.31 shows the droplet trajectories in the housing for the above cases. The only difference between the cases is the droplet diameter, a) 0.01 mm b) 0.05 mm c) 0.1 mm d) 0.15 mm. As could be concluded from the results plotted in Figure 4.30, smaller droplets followed the air flow more, and thus, more water entered the filter. Whereas the larger droplets fell towards the bottom of the housing and created film. One case was also simulated with a mass flow rate of air of 50 liters/s corresponding to the air velocity of 1.78 m/s, which resulted in 61 % of water accumulation in the filter.

As for the simplified domain, a small margin of error should be taken into consideration since both the water in the filter and the water passing the into the housing are taken at a solution time of three seconds. If given enough time, some of the droplets in housing would enter the filter.

The complete air intake was also simulated with the grille. Seen in the previously conducted experiments, the droplets collide with the grille to create a water film, the film then breaks up into droplets again. As mentioned in Section 3.2.8, this was done to investigate if the Fluid Film model is able to replicate the physics. Concluded from this test was that the fluid film and stripping model can be used to model the behavior of the droplets and film at the grille. However, how well it agrees with real behavior can be questioned and further investigation is necessary.

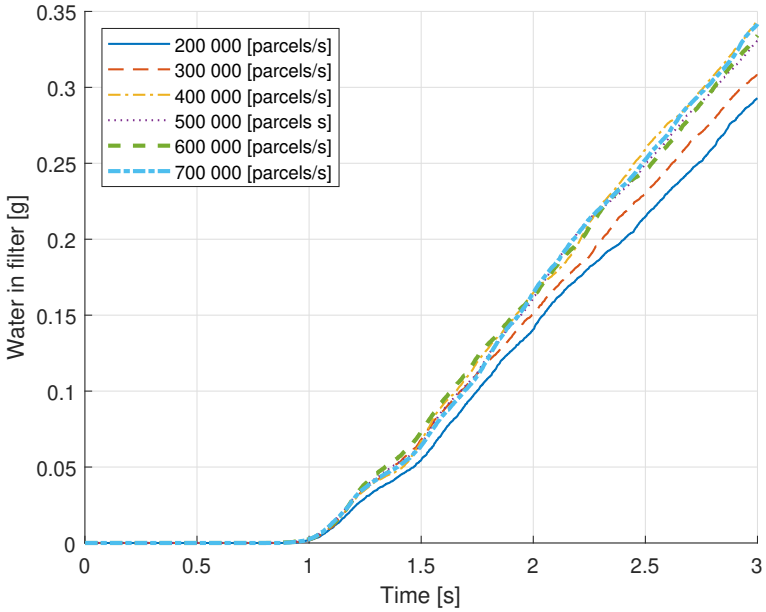

Figure 4.28: Mass of water accumulated in the filter for the complete air intake with respect to time for different numbers of parcels. As seen in the figure, at least 400 000 parcels/s are needed to get a statistically converged result.

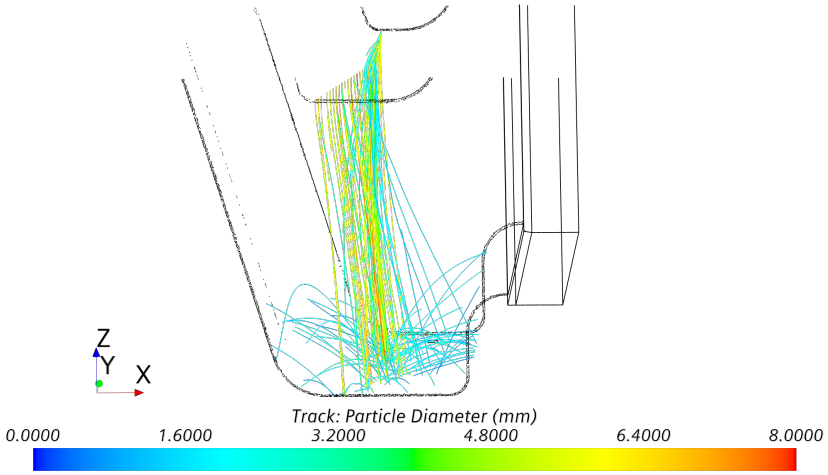

Figure 4.29: Trajectories of the droplets injected at the same location as the stripping occurs in the videos of the previously conducted experiment at Volvo.

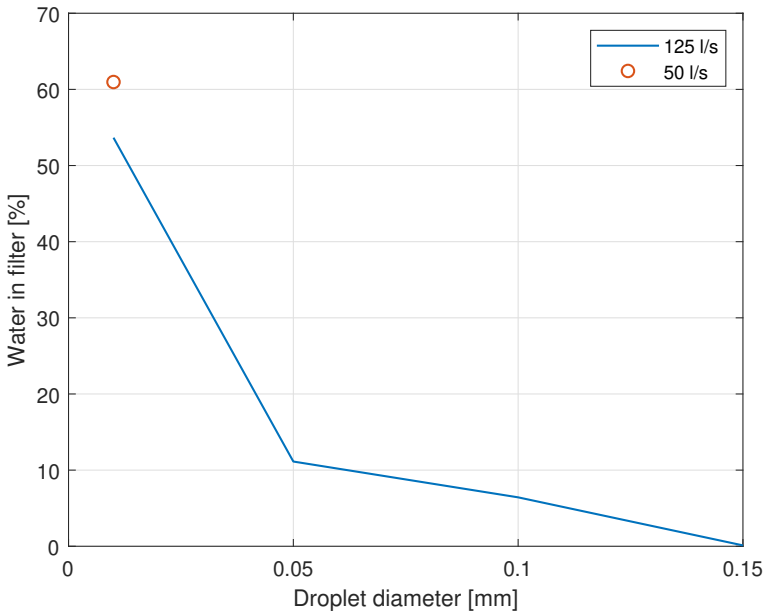

Figure 4.30: Accumulated water in the filter after three seconds for varying droplets diameters and air volume flow rate.

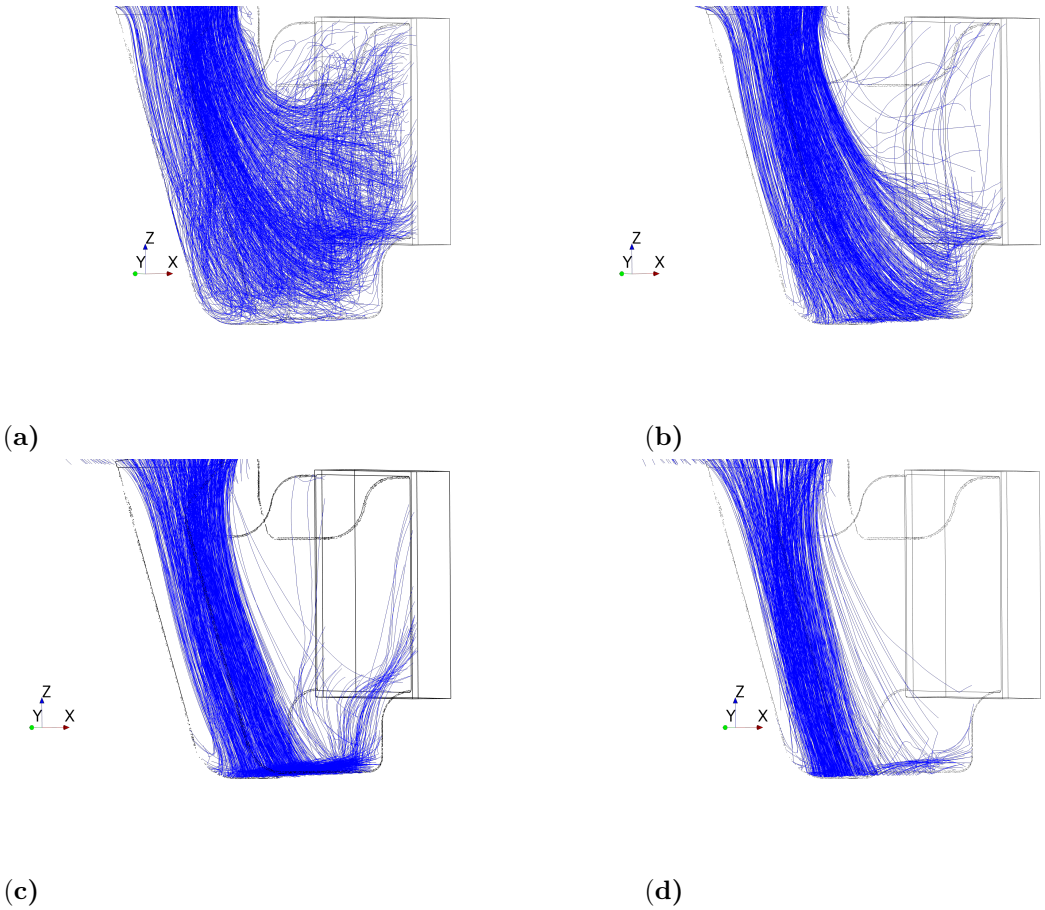

Figure 4.31: Droplet trajectories in the housing with 4.44 m/s at the fan suction boundary, 20 g/s of water injected using a) 0.01 mm droplets b) 0.05 mm droplets c) 0.1 mm droplets d) 0.15 mm droplets.

4.2 Dispersed Multiphase Model

The Dispersed Multiphase model was tested to evaluate if it is a good alternative to the LMP model and whether it is possible to reduce the computational cost of the simulations. Data from the case with mass flow rate 20 g/s water and a volume fraction of $1.6 * 10^{-4}$ is plotted in Figure 4.32. For the one-way coupled simulations, the results from the DMP and LMP simulation are similar. The DMP results showed however a bit lower mass flow rate of water into the housing compared to the LMP. The mass flow rate into the filter was almost identical. However, for the case with two-way coupling, the results are not the same. The LMP simulation resulted in significantly less water into housing and filter.

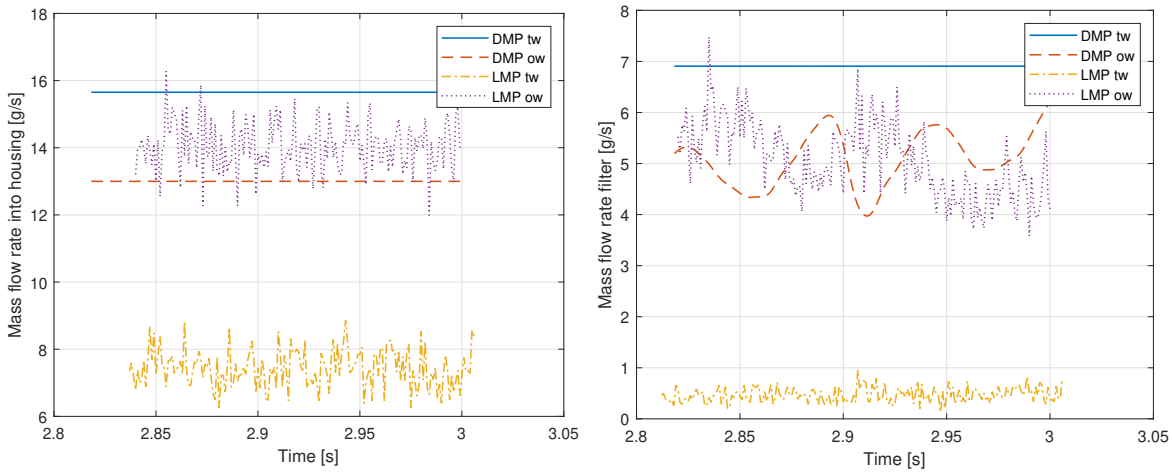

(a) **(b)**

Figure 4.32: The mass flow rate of water for DMP and LMP simulation into a) housing b) filter. Mass flow rate of water into domain: 20 g/s. (tw = two-way coupled, ow = one-way coupled).

Data from the same case simulated with a lower volume fraction of $3 * 10^{-8}$ are plotted in Figure 4.33. The data shows as expected that the water droplets are not affecting the air because of the low volume fraction. Thus, results from the one-way coupled and two-way coupled simulations are identical. The amount of water that flows into the housing for the DMP simulation is very similar to the LMP simulation. However, there is a significant difference in how much water that reaches the filter. The DMP one-way coupled case was also re-simulated with secondary gradients and 2nd order convection scheme for segregated flow, but with no difference in the result.

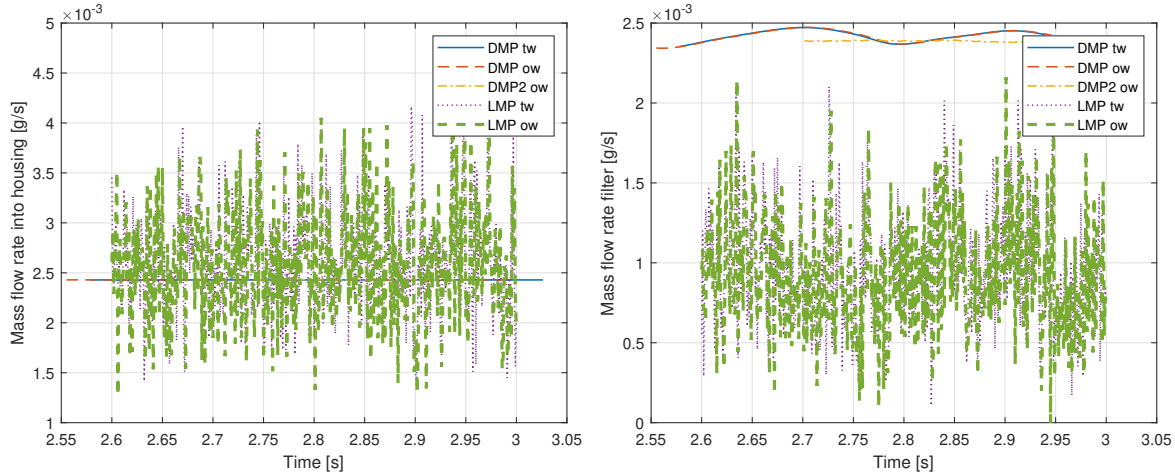

(a) **(b)**

Figure 4.33: The mass flow rate of water for DMP and LMP simulation into a) housing b) filter. Mass flow rate of water into domain: 0.00375 g/s (tw = two-way coupled, ow = one-way coupled, DMP2 = with secondary gradients and 2nd order convection scheme for segregated flow).

Attempts were made to simulate the DMP simulations with 2nd order convection scheme and 2nd order temporal discretization but without success. All simulations with 2nd order schemes had divergence problems, despite low under-relaxations factors.

In Figure 4.34a the particle trajectories are plotted for the one-way coupled case with low volume fraction. Notice that the droplets are removed before reaching the filter. In Figure 4.34b is the same case plotted but simulated with the DMP model. As seen when comparing the two figures are the droplets mainly following the same path, but the DMP droplets seem to be spread out over a larger area compared to the droplets in the LMP simulation.

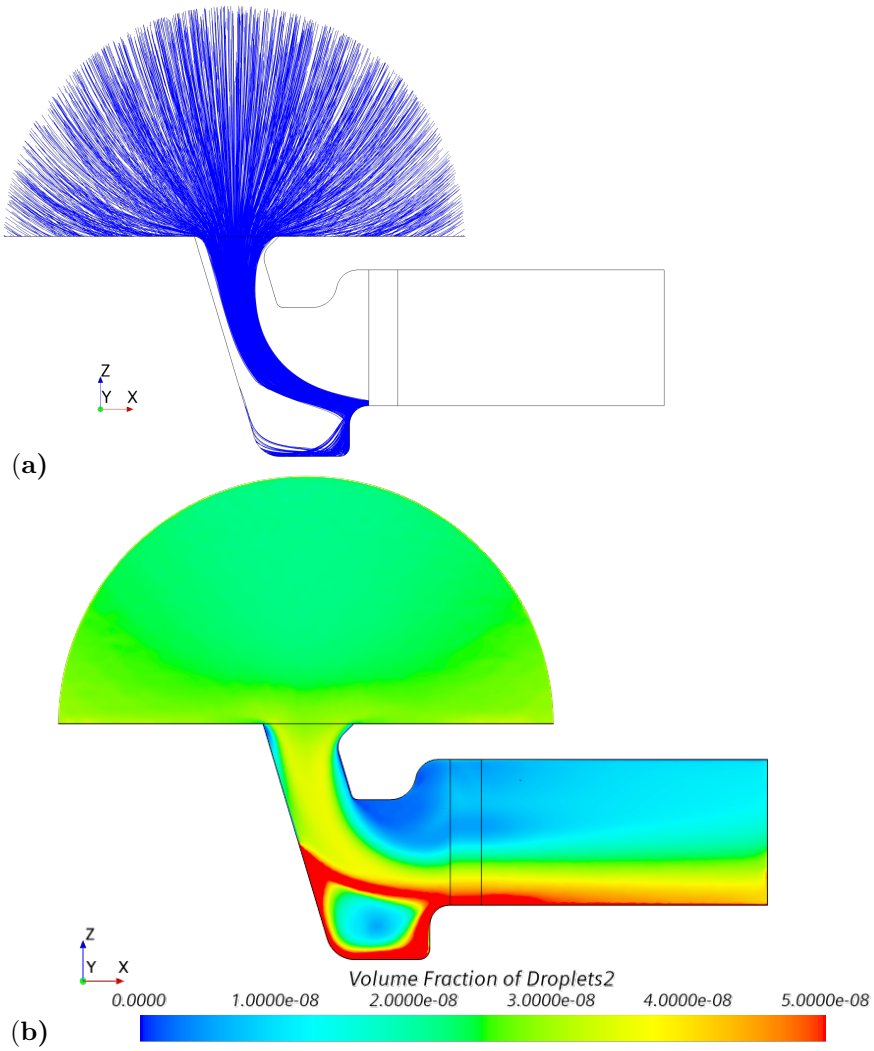

Figure 4.34: Comparison between LMP and DMP. a) Particle trajectories, LMP simulation. b) Volume fraction of water, DMP simulation. The droplets mainly following the same path, but the DMP droplets are spread out over a larger area compared to the droplets in the LMP simulation.

A mesh study was conducted to be sure that the mesh was fine enough. In Figure 4.35 a comparison of the velocity profile in z-direction for the different meshes can be seen. The positions of the probe lines were as illustrated in figure 3.4. In Figure 4.35a, the velocity of the air is plotted and in Figure 4.35b, the velocity if the droplets are plotted. The velocity profiles for the air are almost identical between the meshes, but for the droplets, there are small differences between the meshes. However, for a base size of 8 mm or smaller, the velocity profile of droplets are almost identical.

In Figure 4.36, the velocity profile of the air and droplets are plotted at line probe 2 for the different volume meshes. As seen, the profiles are again very similar between the meshes both for the air and for the droplets. As before, the variance for the droplets are a bit larger than for the air and the velocity peak at z=1.38 m is significantly lower for the coarsest mesh.

The velocity profiles were in general very similar between the meshes. However, the mass of water that was accumulated in the filter was varying more. In Figure 4.37 is the mass flow rate of water into filter plotted during a time interval when the mass flow rate has become relatively steady. The difference between the coarse mesh and the finest mesh is around 15 %. Even the difference between the mesh used before, with a base size of 8 mm, is almost 8 %. The mass flow rate for the two meshes with the smallest base size is similar. Therefore, a finer mesh should have been used in the study before. However, even with the finest mesh, the results would have been different from the LMP simulations when compared to the results in Figure 4.33.

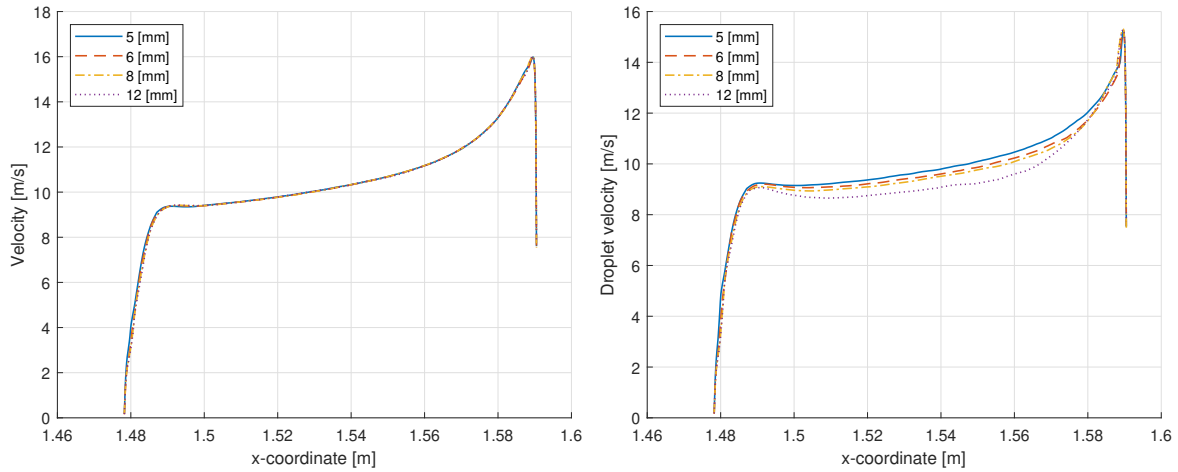

(a) **(b)**

Figure 4.35: The velocity of the a) air b) droplets, in the negative z-direction with respect to x-coordinate in the housing at line probe 1 for varying volume mesh sizes.

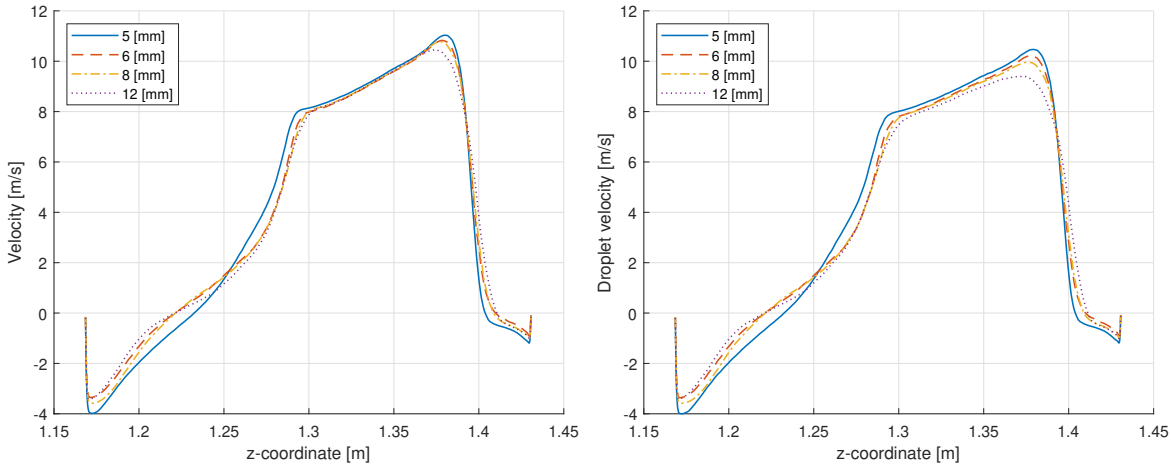

(a) (b)

Figure 4.36: The velocity of the a) air b) droplets, in the x-direction with respect to z-coordinate in the housing at line probe 2 for varying volume mesh sizes.

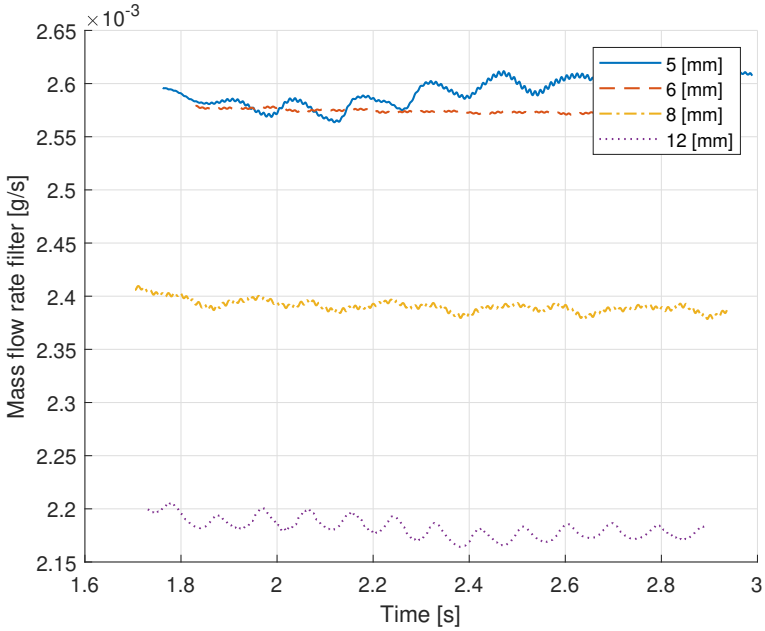

Figure 4.37: The mass flow rate into the filter for varying volume mesh.

5 Conclusions

The objective of this project was to develop a simulation methodology at Volvo Technology to simulate water separation in automotive air intake systems. The method would decrease the needs of experiments and also make it possible to optimize the geometry before any prototypes are built. Several simulation models in STAR-CCM+ were examined to evaluate if they are suitable to model the physics that are involved in water separation.

The Lagrangian Multiphase model (LMP) offers several advantageous functionalities for simulation of water separation in the air intakes. It is possible to follow the trajectories of the droplets, which is important to get an understanding of how the droplets behave in air intake systems. Furthermore, LMP is compatible with more developed physics models such as impingement and stripping than for example Dispersed Multiphase model (DMP).

To model the water film on the walls, both the Fluid Film model and Volume of Fluid (VOF) were examined. Due to the fact that VOF is more computationally expensive, the Fluid Film model is recommended. The Fluid Film model seemed to work well for this case, but a validation against experiments is necessary.

The Bai-Gosman model used for the impingement from Lagrangian droplets to the fluid film is not dependent on the surface mesh. However, if too small cells are used, an unphysically thick film can occur and cause divergence problems. This can be solved by limiting the fluid film thickness, but this is also unphysical since the fluid film that exceeds the film thickness limit is removed from the simulation. The limit used for the fluid film thickness was 10 mm. Only when using small surface cell sizes in the mesh independence study the film thickness exceeded the limit. With the final mesh, no fluid film was removed due to the limit, and thus, the conservation of mass was satisfied. The wave stripping model is highly dependent on the surface mesh size. The surface mesh affects both the time when the stripping occurs and the rate of the stripping. Therefore, if the stripping of droplets is important, the behavior and the rate of stripping needs to be checked for each case to be sure that the behavior matches validated data.

Small time steps are recommended, but if 2nd order time discretization scheme is used, it can be increased to 1 ms. Larger time step than 1 ms may be possible with the 2nd-order time discretization but was not tested.

In a previous experiment conducted at Volvo, a water mass flow rate of 25 g/s was used. This resulted in such a high volume fraction that the droplets impact on the air cannot be neglected. Therefore, two-way coupling is needed to replicate the experiment with simulations. However, if the purpose is to replicate rain, the volume fraction becomes so low that the droplets impact on the air is negligible. In that case, one-way coupling is sufficient. One-way coupling will significantly lower the computational power needed for the simulation. One drawback when using one-way coupling with the Lagrangian Multiphase model is that the water mass transfer with the fluid film is not possible, thus, no fluid film will be created by impinging droplets. Therefore, one-way coupling is not possible to use if the fluid film is of importance.

The volume fraction of water has a huge effect on the percentage of injected water that accumulates in the filter for some droplets diameters. It may, therefore, be needed to test different volume fractions to be able to validate that the air intake fulfills the requirements. During experiments this effect needs to be taken into consideration. The difference in how high percentage of water that flows into the filter can be explained by if there are enough droplets to influence the air flow. For the higher mass rates of water there are enough droplets to influence the air flow and therefore are the droplets trajectories changed as well.

The amount of water that follows the air into the filter is highly dependent on the droplet diameter for the simplified domain, as well as the complete air intake domain. The current air intake design separates droplets larger than 0.1 mm well. But for smaller droplets sizes the separation does not work very well and the percentage that follows the air into the filter is much higher.

Many of the models used in the simulations include random variables, as mentioned in the repeatability study and the stripping parameter study. Ideally, to get reliable results from these studies, an average of the results from a sufficient number of simulations should have been used. However, due to the limitation of computational resources, this was not conducted.

The planned experiment was not performed. Thus, it was not possible to validate the models used in the simulations with experimental data. However, with pictures and videos from an earlier conducted experiment, it was possible to validate where the stripping occurs and also get an approximation of the size of the stripping droplets. By using the LMP model with the Fluid Film model it was possible to capture the physics of water droplets which created a fluid film at the wall and then flowing down the wall to be stripped at the curved edge, just as seen in the videos from the experiment. Unfortunately, no other data is saved from the experiment to

be used to validate the results from the simulations, and thus, there is an uncertainty in how well these models replicate the real conditions.

The results from the DMP simulations did not fully agree with the LMP simulations. The mesh study showed that a finer mesh needs to be used with the DMP model compared to the LMP model. This can be due to how the dispersed phase is calculated. In the DMP model, each cell has a constant volume fraction of droplets. Therefore, will a change in mesh give a more detailed solution of how the droplets are distributed in the domain. In the LMP model, the droplet exists in a certain point and the forces are interpolated to the droplet.

There were also divergence problems with the DMP model and therefore was a 1st order convection scheme for the dispersed phase and 1st order time discretization was used. This may have smeared out the droplets in the air. The simulations were carried out with a droplet diameter that partially followed the air into the filter. That explains why the difference is so significant between the DMP and the LMP simulations, a small difference in the flow results in a large difference in how much water that is accumulated in the filter. Except for the difference in how much the droplets are spread, the trajectories of the droplets seem to be similar between the DMP and LMP model. If a larger or smaller droplet size would have been simulated the results would have been more similar, but that would have been less interesting to simulate.

The DMP model is more difficult to validate with an experiment at Volvos test rigs, since it is not possible to inject water droplets with an injector. The impingement and stripping models are also less advanced compared to the LMP model. Since the time used to investigate the DMP model was much shorter than for the LMP model. There are several things that still needs to be investigated before using the DMP model for simulation of water separation in the air intakes.

5.1 Suggestions for further research

To know if the recommended models and methods are accurate enough to simulate and capture the physics of water separation in automotive air intakes it is necessary to validate the models with experiments. The percentage of water accumulated in the filter needs to be measured and compared. This is the most important parameter. However, it is also suggested that the other STAR-CCM+ models used and recommended are compared and validated against experiments. For example the Fluid Film model, wave stripping, impingement, etc.

One of the limitations of this project was that only the flow inside and just outside the air intake inlet was taken into account. However, the aerodynamics around the whole truck will affect the flow inside the air intake. In this project, the boundary at the bottom of the inlet hemisphere was set to walls with a slip condition for the air, which is unphysical. Thus, the logical next step is to take the flow outside the air intake into account.

The VOF model was not possible to use to solve the fluid film in the air intake, because of the limitations with the stripping model. However, in STAR-CCM+ there is another model called Resolved Fluid Film. This model is a combination of the Fluid Film model and VOF. The Resolved Fluid Film model can be an alternative when solving the film in more complicated geometries as for the grille. Therefore, it is suggested to test how well this model works in such cases.

The DMP model was not investigated as thoroughly as the LMP model and substantial differences could be seen between the DMP and LMP model. Thus, more research needs to be done on this model to optimize it.

References

[1] C. Bai. Modelling of spray impingement processes. (1996).

[2] C. Bai and A. Gosman. Development of methodology for spray impingement simulation. *SAE transactions* (1995), 550–568.

[3] C. Bai, H. Rusche, and A. Gosman. Modeling of gasoline spray impingement. *Atomization and Sprays* **12**.1-3 (2002).

[4] L. Davidson. Fluid mechanics, turbulent flow and turbulence modeling. *Chalmers University of Technology, Goteborg, Sweden* (2020).

[5] M. A. Friedrich et al. A separation criterion with experimental validation for shear-driven films in separated flows. *Journal of Fluids Engineering* **130**.5 (2008).

[6] S. A. Ghani, A. Aroussi, and E. Rice. Simulation of road vehicle natural environment in a climatic wind tunnel. *simulation practice and theory* **8**.6-7 (2001), 359–375.

[7] A. Gosman and E. Loannides. Aspects of computer simulation of liquid-fueled combustors. *Journal of energy* **7**.6 (1983), 482–490.

[8] T. Hagemeier, M. Hartmann, and D. Thévenin. Practice of vehicle soiling investigations: A review. *International Journal of Multiphase Flow* **37**.8 (2011), 860–875.

[9] K.-Y. Law and H. Zhao. *Surface wetting: characterization, contact angle, and fundamentals*. Springer Switzerland, 2016.

[10] F. Maroteaux et al. Liquid film atomization on wall edges—separation criterion and droplets formation model. *J. Fluids Eng.* **124**.3 (2002), 565–575.

[11] D. K. F. Mechanics. *Frank M. White*. 2010.

[12] K. Meredith et al. A numerical model for partially-wetted flow of thin liquid films. *Computational Methods in Multiphase Flow VI* **70** (2011), 239.

[13] I. Nezu and W. Rodi. Open-channel flow measurements with a laser Doppler anemometer. *Journal of hydraulic engineering* **112**.5 (1986), 335–355.

[14] P. O'rourke and A. Amsden. A particle numerical model for wall film dynamics in port-injected engines. *SAE transactions* (1996), 2000–2013.

[15] Regndroppars utseende (2015). URL: `https://www.smhi.se/kunskapsbanken/meteorologi/regndroppars-utseende-1.4657` (visited on 04/28/2020).

[16] S. Sasic. "Lecture notes for the Multiphase flow course (TME160)". 2019.

[17] J. D. Schwarzkopf et al. *Multiphase flows with droplets and particles*. CRC press, 2011.

[18] Siemens. *Simcenter STAR-CCM+ Documentation*. Version 2020.1.

[19] C. D. Stow and M. G. Hadfield. An experimental investigation of fluid flow resulting from the impact of a water drop with an unyielding dry surface. *Proceedings of the Royal Society of London. A. Mathematical and Physical Sciences* **373**.1755 (1981), 419–441.

[20] S. Subramaniam. Lagrangian–Eulerian methods for multiphase flows. *Progress in Energy and Combustion Science* **39**.2-3 (2013), 215–245.